

## ABSTRACT

We here present the first comprehensive provenance study of the Sahara Desert using a combination of multiple provenance proxies and state-of-the-art statistical analysis. Our dataset comprises 44 aeolian-dune samples, collected across the region from 12°N (Nigeria) to 34°N (Tunisia) and from 33°E (Egypt) to 16°W (Mauritania) and characterised by bulk-petrography, heavy-mineral, and detrital-zircon U–Pb geochronology analyses. A set of statistical tools including Multidimensional Scaling, Correspondence Analysis, Individual Difference Scaling, and General Procrustes Analysis was applied to discriminate among sample groups with the purpose to reveal meaningful compositional patterns and infer sediment transport pathways on a geological scale. The overall homogeneity across sand samples, however, precluded a detailed narrative.

Saharan dune fields are, with a few local exceptions, composed of pure quartzose sand with very poor heavy-mineral suites dominated by durable zircon, tourmaline, and rutile. Some feldspars, amphibole, epidote, garnet, or staurolite occur closer to basement exposures, and carbonate grains, clinopyroxene and olivine near a basaltic field in Libya. Relatively varied compositions also characterize sand along the Nile Valley and the southern front of the Anti-Atlas fold belt in Morocco. Otherwise, from the Sahel to the Mediterranean Sea and from the Nile River to the Atlantic Ocean, sand consists nearly exclusively of quartz and durable minerals. These have been concentrated through multiple cycles of erosion, deposition, and diagenesis of Phanerozoic siliciclastic rocks during the long period of relative tectonic quiescence that followed the Neoproterozoic Pan-African orogeny, the last episode of major crustal growth in the region. The principal ultimate source of recycled sand is held to be represented by the thick blanket of quartz-rich sandstones that were deposited in the Cambro-Ordovician from the newly formed Arabian-Nubian Shield in the east to Mauritania in the west. Durability of zircon grains and their likelihood to be recycled from older sedimentary rocks argues against the assumption, too often implicitly taken for granted in provenance studies based on detrital-zircon ages, that their age distribution reflects transport pathways existing at the time of deposition rather than inheritance from multiple and remote landscapes of the past.

Figure 1

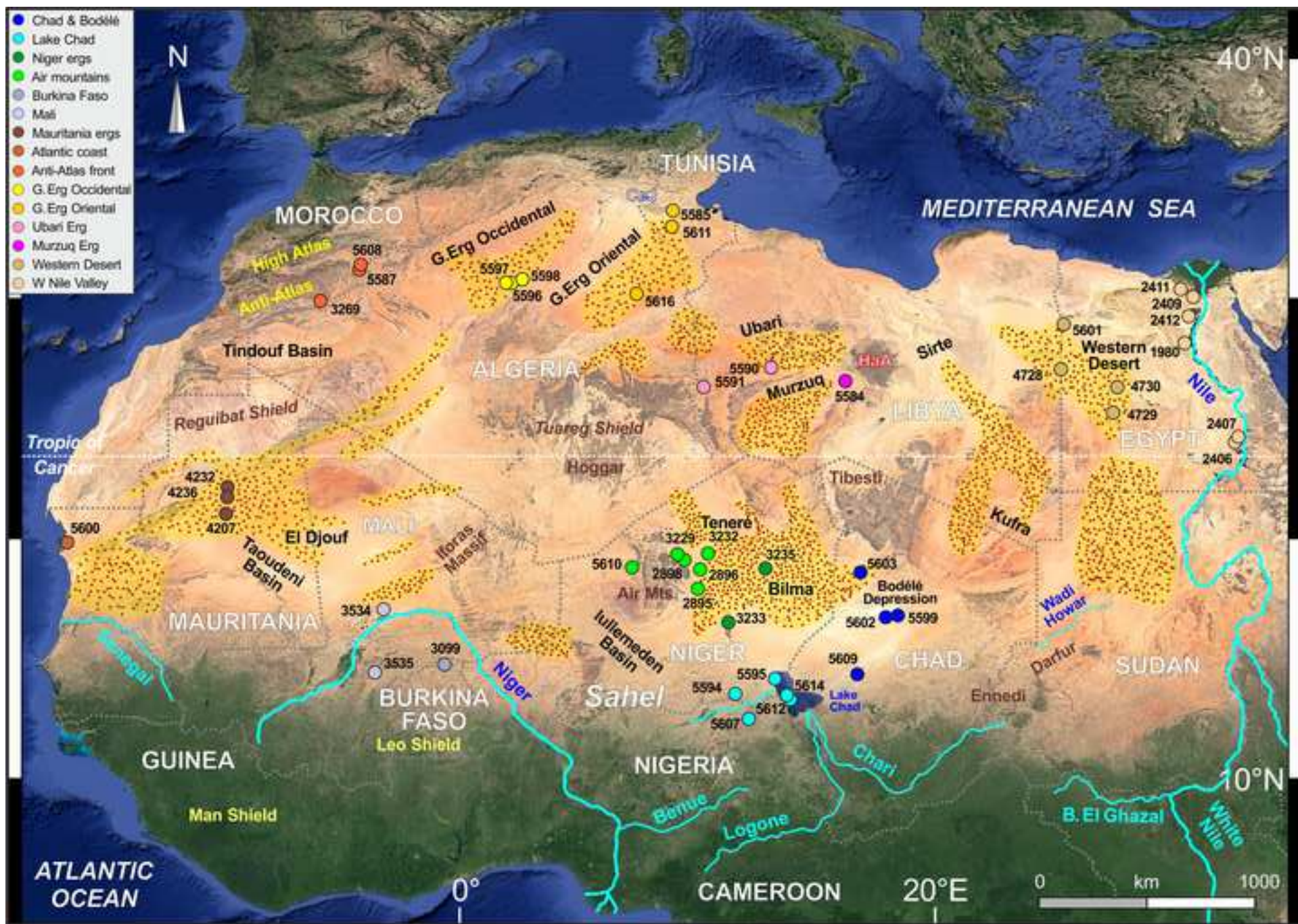
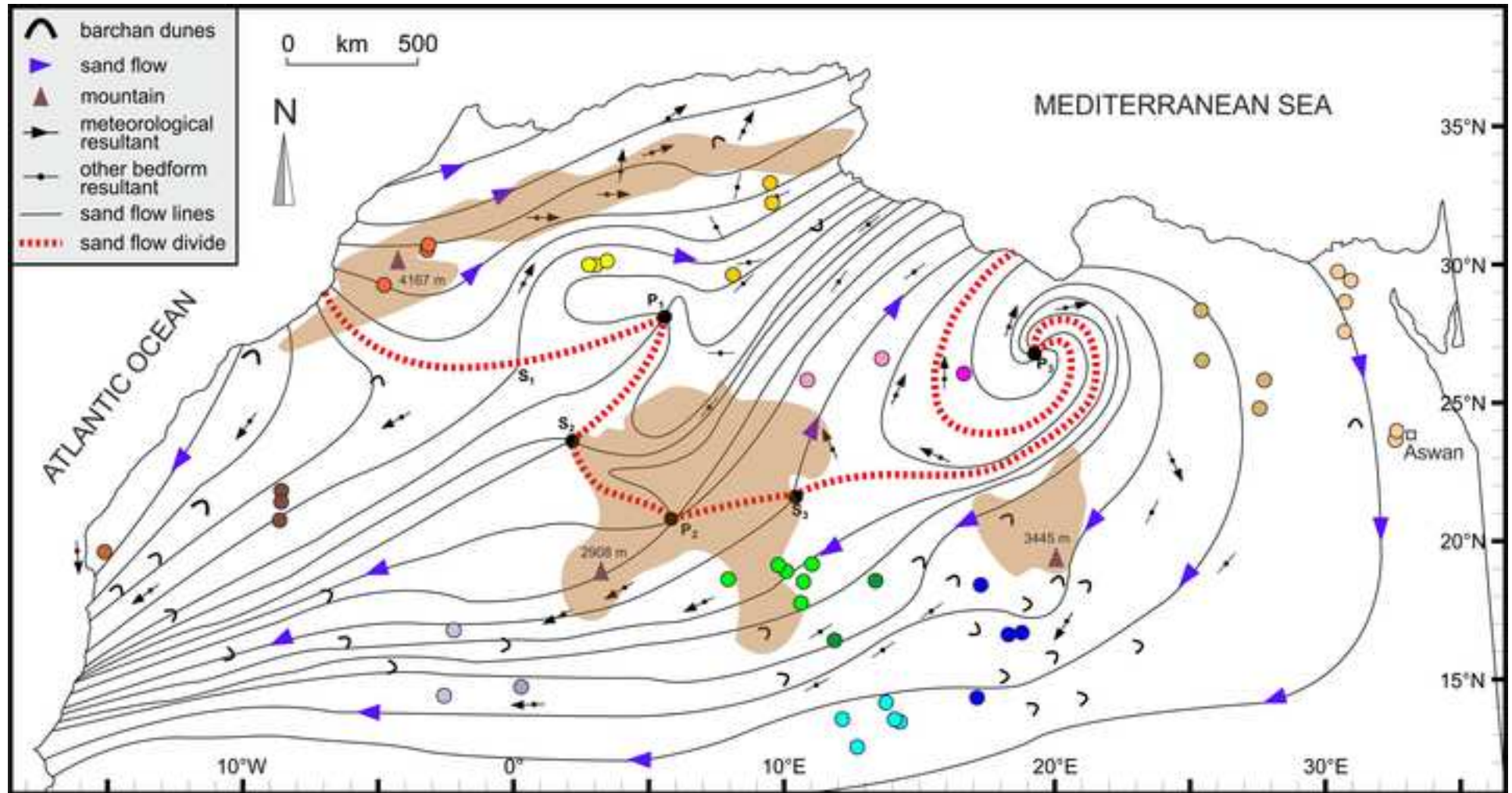
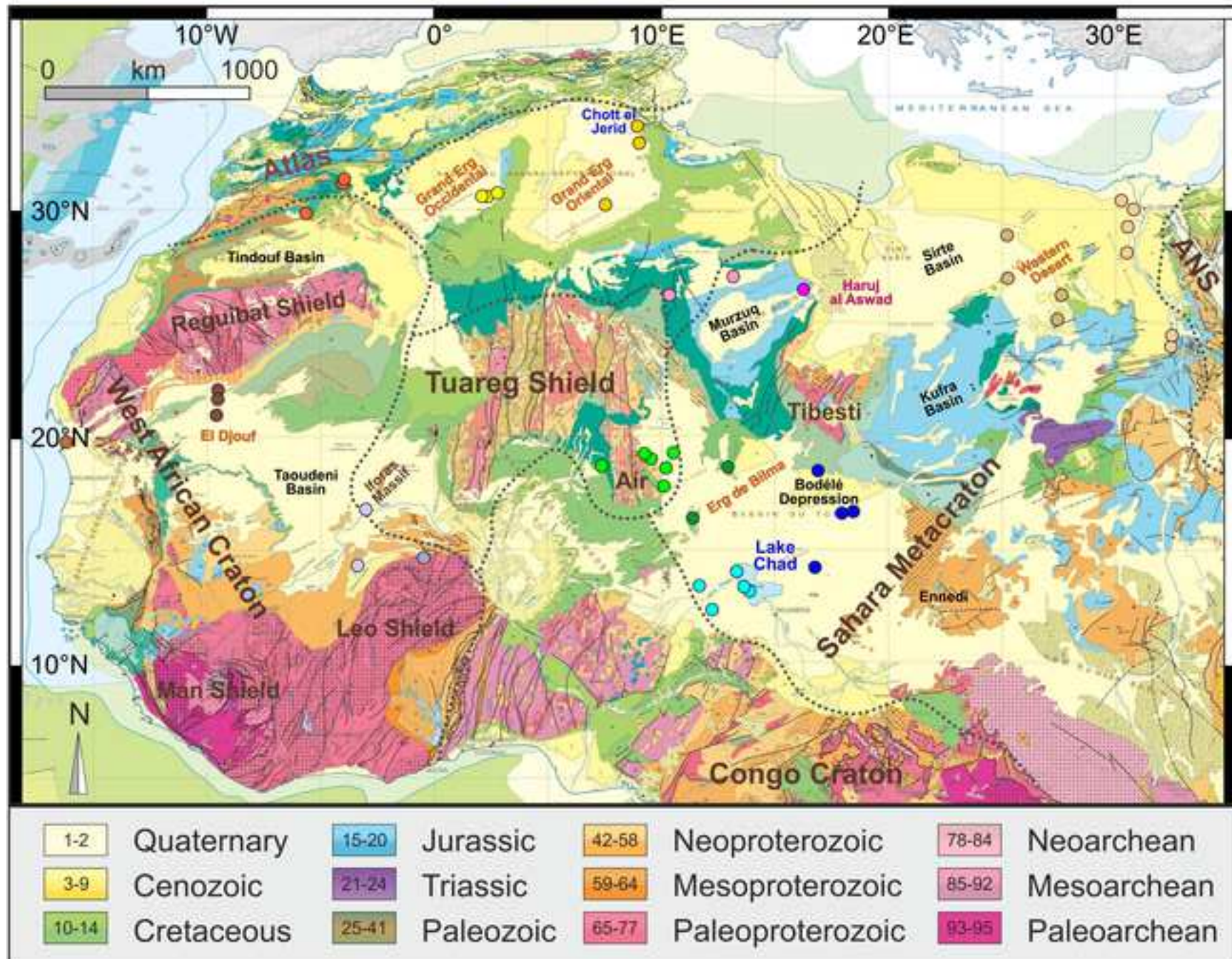




Figure 2









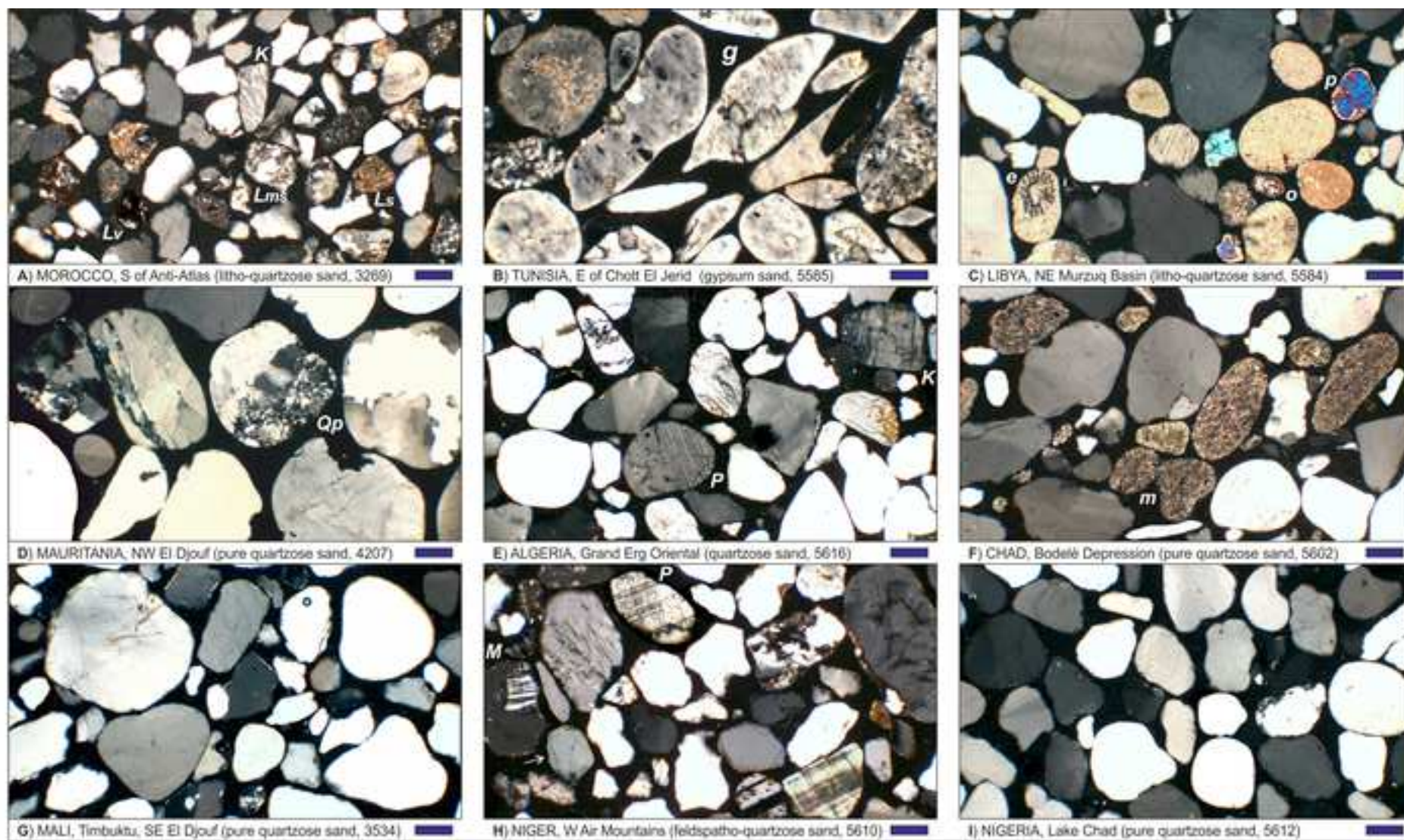


Figure 5

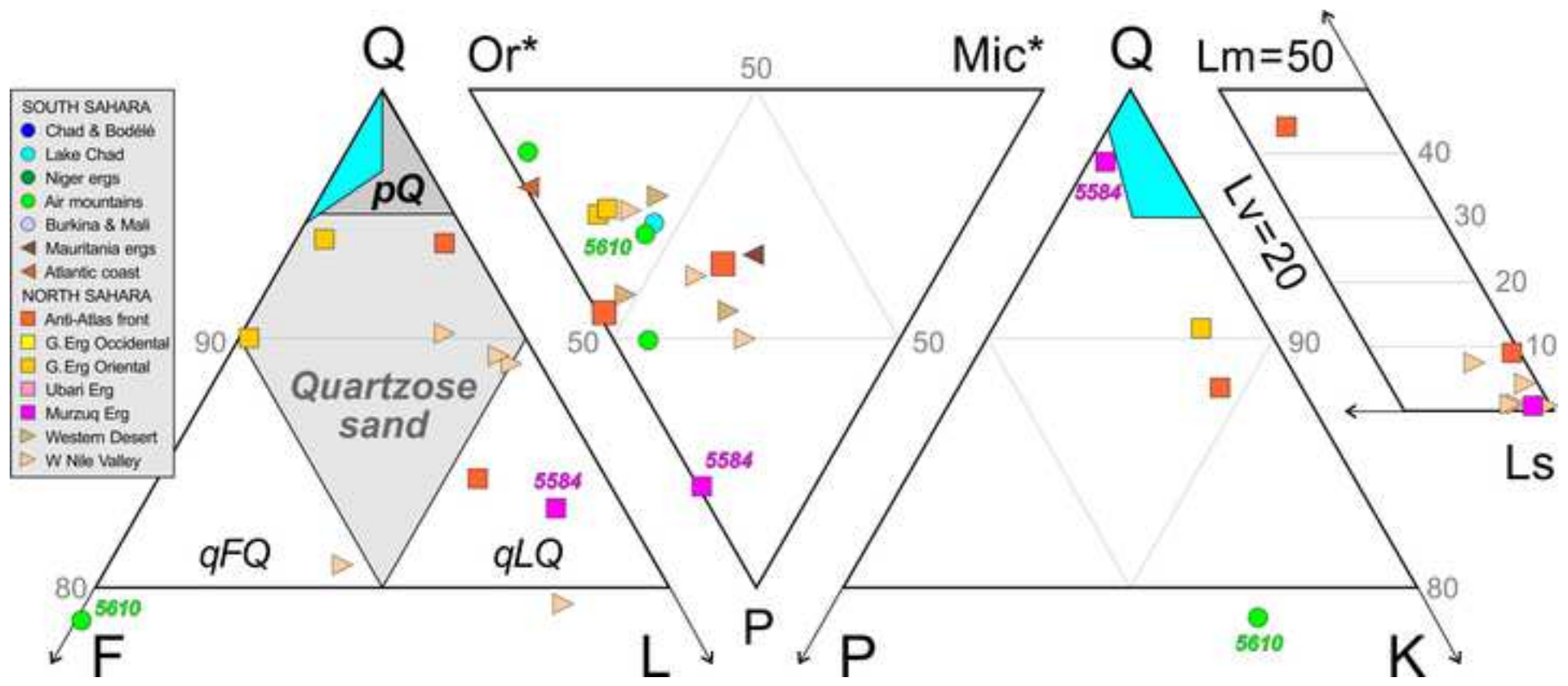




Figure 6

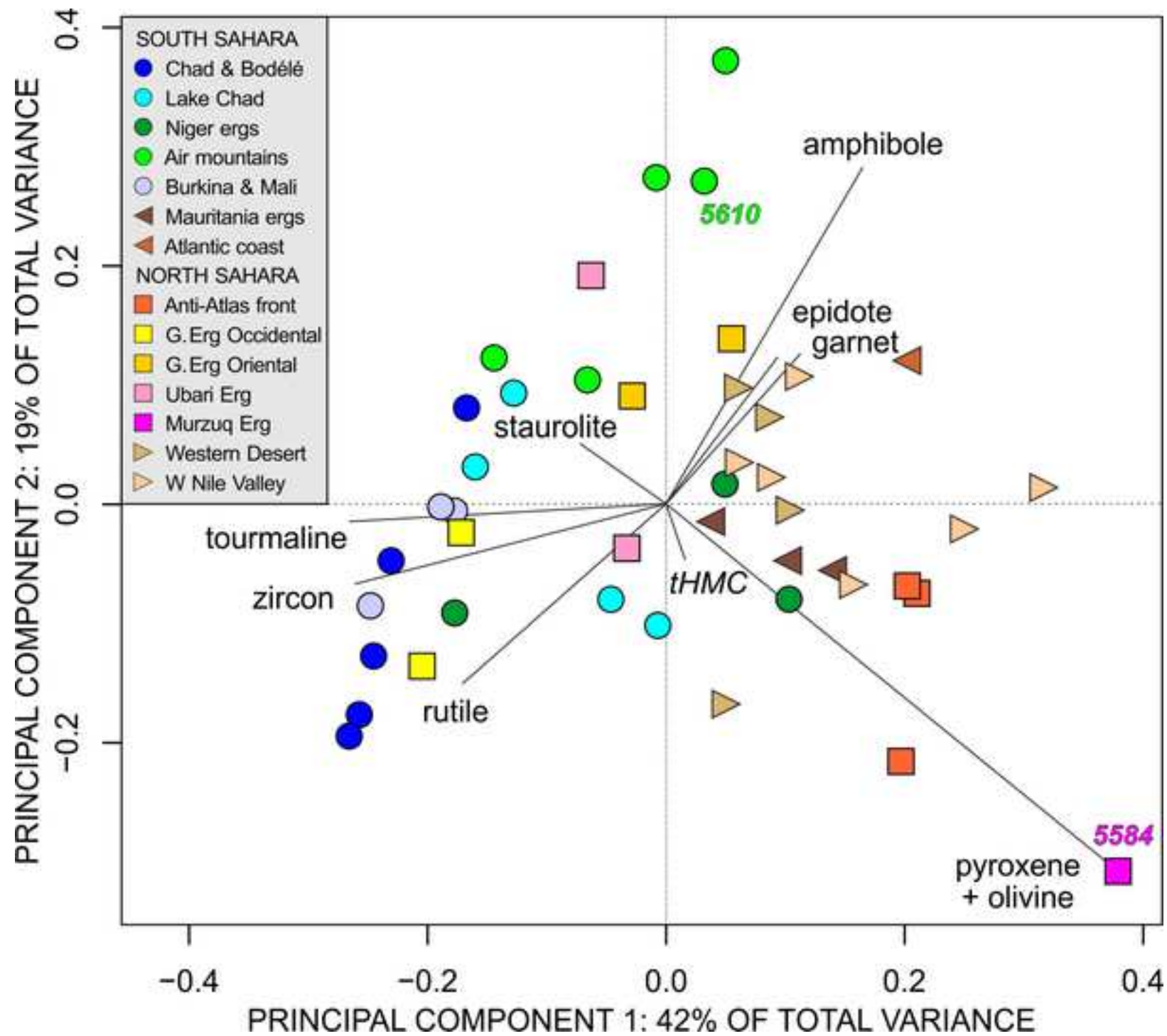


Figure 7

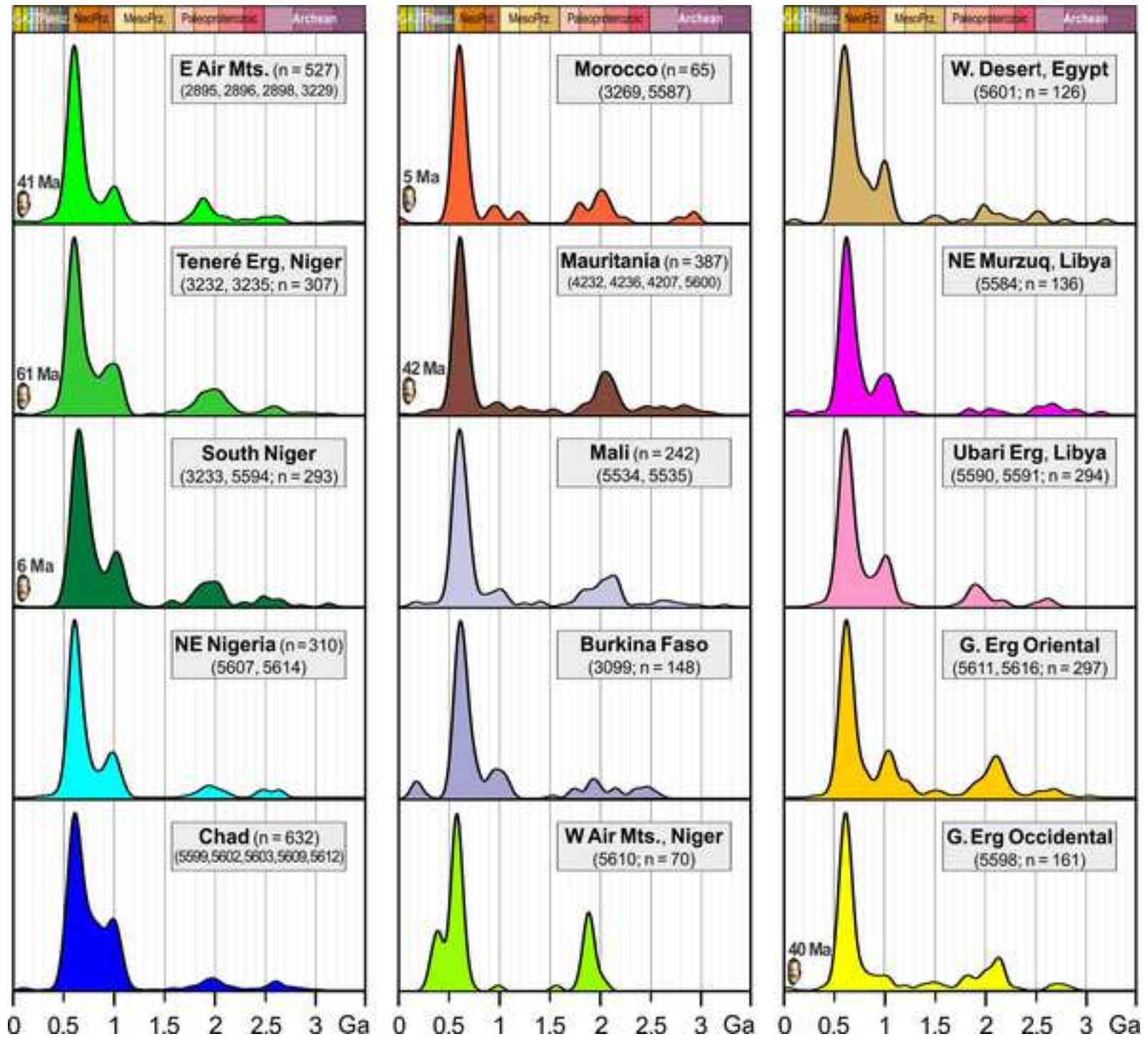
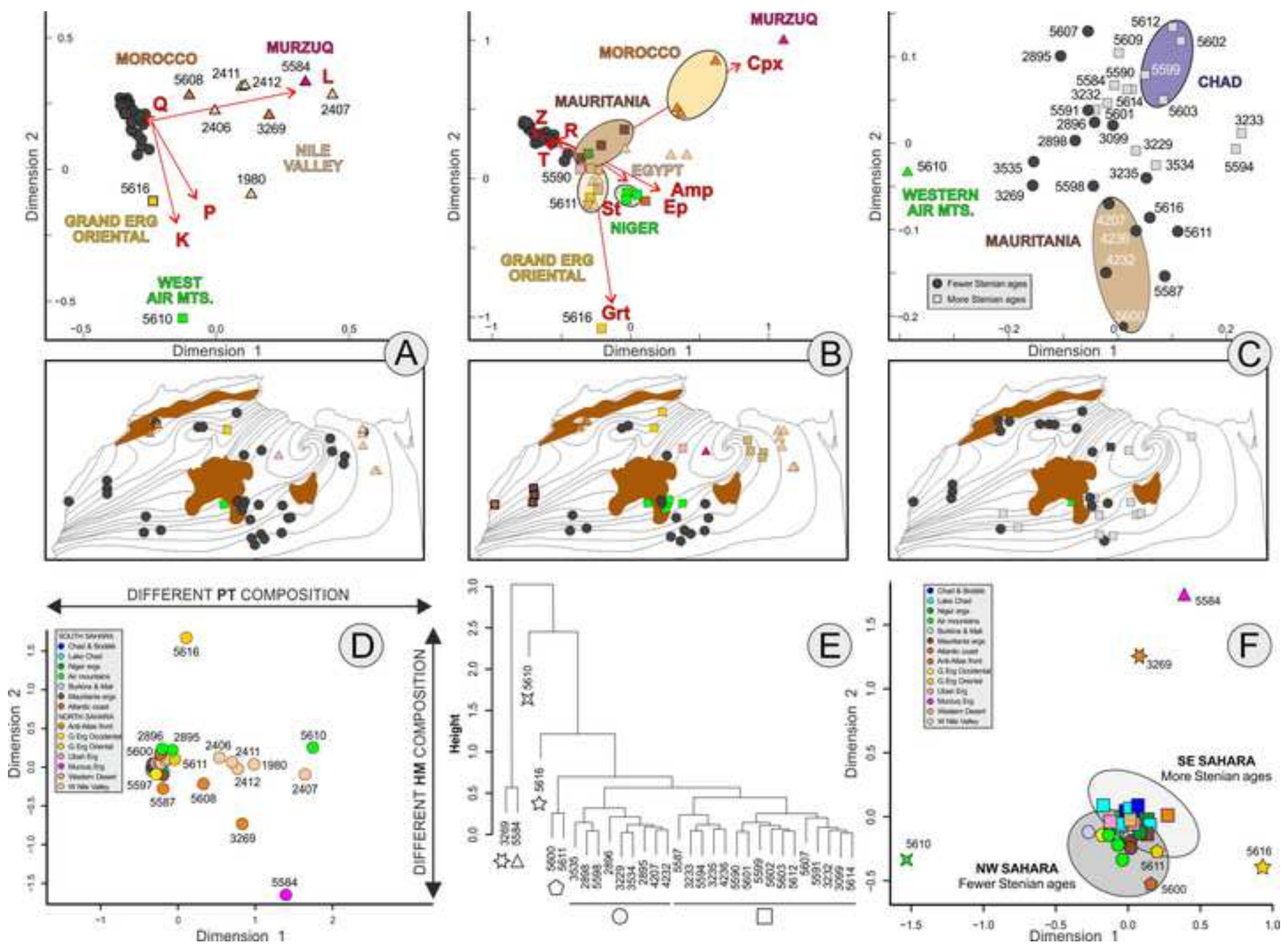
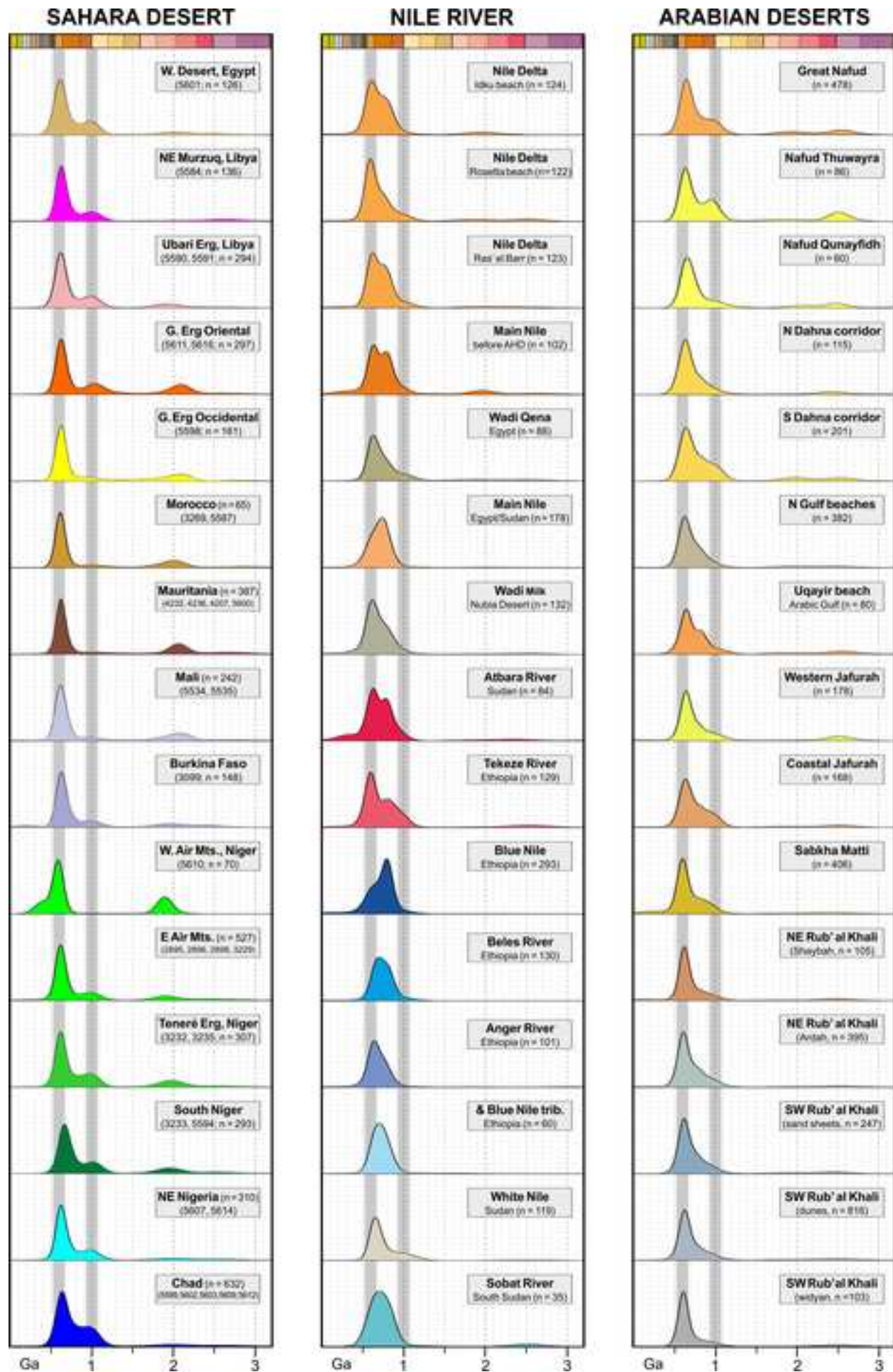




Figure 8

[Click here to access/download;Figure;Figure 8 Sahara Statistics.jpg](#)







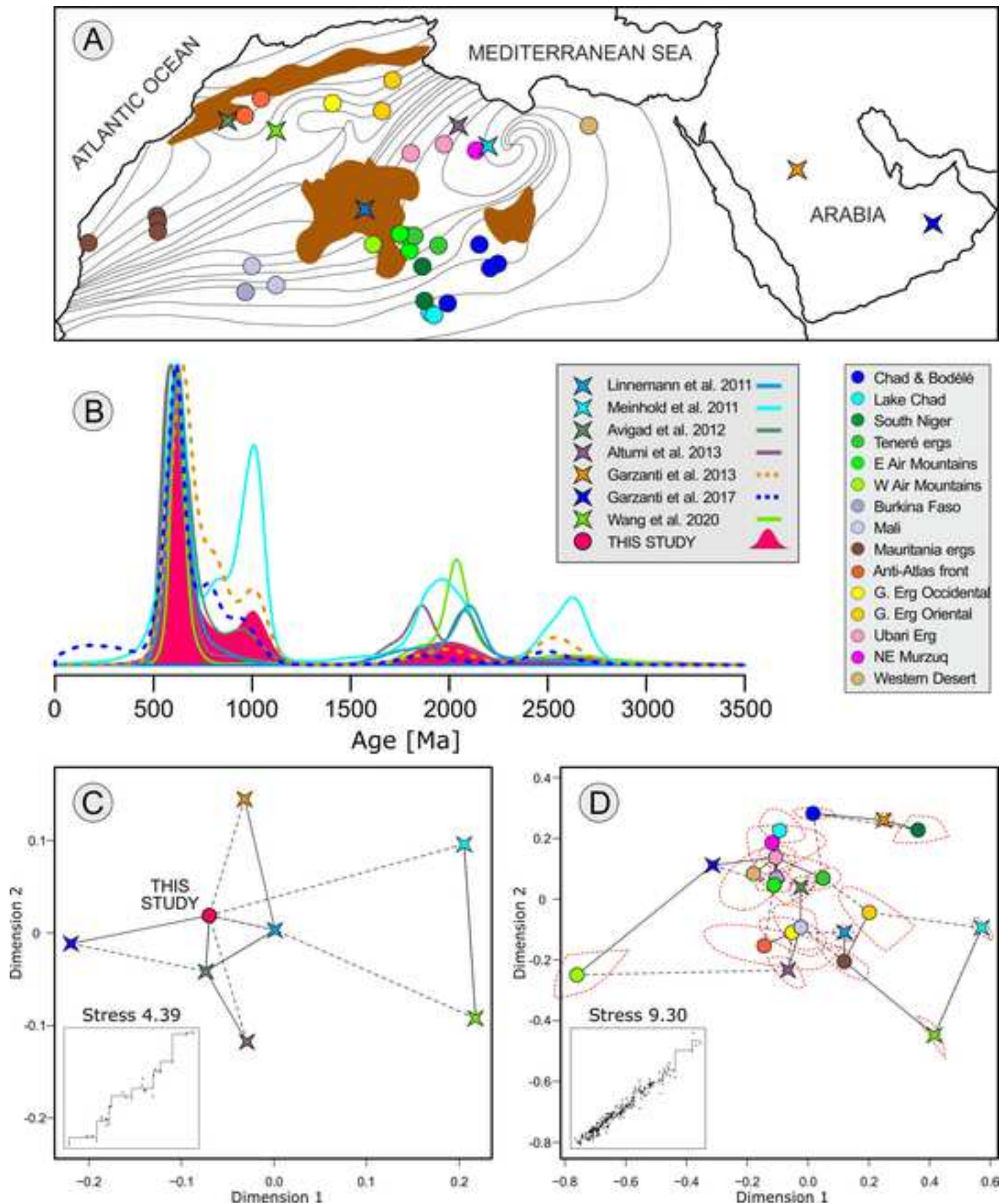


Table 1

[Click here to access/download;Table;Table 1 Sahara PTHM Parameters.xlsx](#)

	n°	Q	F	Lv	Lc	Lsm	total	P/F	tHMC	ZTR	Ap	Ttn	Ep	P&P	Grt	St	Ky	Amp	Px	OI	&tHM	total
CHAD & NIGERIA																						
Bodélé Depression	4	99	0.8	0	0	0.1	100.0	0%	0.1	81	1	2	8	0	1	1	0.3	3	1	0	1	100.0
Lake Chad	4	98	1	0	0	0.5	100.0	54%	0.2	89	1	0.6	2	0	0.3	4	0.7	0.7	0	0	2	100.0
NIGER, BURKINA, MALI																						
Southern Niger	2	99	0.4	0	0	0.2	100.0	0%	0.3	94	0.2	1	1	0	0.2	1	0	0.2	0	0	1	100.0
Erg de Bilma	2	98	1	0	0	0.5	100.0	58%	0.2	60	0.5	1	13	0	7	2	0	6	9	0	0.2	100.0
E Air Mountains	2	99	0.7	0	0	0.3	100.0	0%	0.1	69	0.5	0.5	7	0	0	10	0	11	0.2	0	2	100.0
SE Air Mountains	2	96	4	0	0	0.1	100.0	31%	0.2	24	1	3	20	0	2	10	0	40	0	0	0.2	100.0
W Air Mountains	1	79	21	0	0	0	100.0	29%	0.2	23	4	1	16	0	1	1	1	52	0	0	0.5	100.0
Burkina Faso	1	100	0	0	0	0.2	100.0	n.d.	0.2	77	0	0	20	0	0	2	0	0.5	0	0	0	100.0
Mali	2	100	0.2	0	0	0	100.0	50%	0.1	91	0.2	0.5	3	0	0	3	1	0.5	0	0	0.5	100.0
MAURITANIA																						
Coastal Mauritania	1	97	3	0	0	0	100.0	33%	1.2	16	0.5	0.5	35	0	6	1	0	35	4	0	2	100.0
NW El Djouf	3	99	0.8	0	0	0.3	100.0	10%	0.1	50	1	0.4	21	0	4	4	0	5	13	0	1	100.0
MOROCCO & ALGERIA																						
Anti-Atlas	3	92	3	0.6	1	4	100.0	43%	0.3	19	1	3	11	12	2	2	0	9	38	0	3	100.0
Grand Erg Occidental	2	99	0.6	0	0	0	100.0	33%	0.1	93	0.2	0.4	5	0	2	0	0	0	0	0	0.2	100.0
Grand Erg Oriental	1	90	10	0	0	0.2	100.0	24%	0.6	20	0	1	7	0	64	1	1	0	0	0	5	100.0
TUNISIA & LIBYA																						
Grand Erg Oriental	1	94	5	0	0.5	0.5	100.0	25%	0.3	44	0.4	4	16	0	12	1	1	17	1	0	3	100.0
Ubari Erg	2	99	1	0	0	0	100.0	10%	0.3	72	0	1	11	0	3	1	0	10	1	0	1	100.0
NE Murzuq Erg	1	83	2	0.2	14	0.7	100.0	80%	1.1	2	0	0	2	0	0.5	0	0	0.5	56	38	1	100.0
EGYPT																						
Western Desert	4	97	3	0	0.3	0.2	100.0	39%	0.1	44	1	2	23	0	11	5	1	6	5	0	1	100.0
Aswan area	2	85	3	0.3	9	2	100.0	44%	1.5	11	0	0.2	30	0	2	3	0.7	29	23	0	1	100.0
Nile Valley	4	89	4	0.4	4	2	100.0	41%	0.8	36	0.1	1	26	0	7	10	4	9	6	0	0.2	100.0



Study	Unit	Technique	concordant/ total ages	Age clusters	$\epsilon\text{Hf}(t)$ values
Linnemann et al. 2011	Cambro-Ordovician Tassili Ouan Hoggar, Algeria	U-Pb (LA-ICP-MS)	630/850	0.74-0.54 (61%), 2.2-2.0 (20%), 1.8-1.3 (7%), 0.98-0.75 (6%), 2.65-2.30 (3%)	
Meinhold et al. 2011	Paleozoic-Mesozoic Murzuq, Libya	LA-SF-ICP-MS	1257/1678	0.72-0.53 (39%), 1.06-0.92 (18%), 2.2-1.7 (16%), 2.75-2.50 (8%)	
Avigad et al. 2012	Lower and Middle Cambrian, Morocco	LA-ICP-MS/Lu-Hf	419/?	<b>Mid.Cambrian:</b> 0.63-0.54 (18%), 1.00-0.63 (61%), 1.2-1.0 (3%), 2.5-1.6 (16%) <b>Lower Cambrian:</b> 0.63-0.54 (71%), 1.00-0.63 (5%), 2.5-1.6 (23%)	<b>Neoproterozoic zircon:</b> <b>LC:</b> $\epsilon\text{Hf}(t) > 0$ ; <b>MC:</b> $\epsilon\text{Hf}(t) < 0$
Altumi et al. 2013	Cambrian Hasawnah Fm., Libya	LA-ICP-MS	329/720	0.70-0.54 (60%), 2.4-1.6 (18%), 3.4-2.5 (5%)	
Wang et al. 2020	Cambrian, Ougarta Mountains, Algeria	LA-ICP-MS/Lu-Hf	449/536	0.80-0.56 (49%), 1.47-0.89 (2.4%), 3.4-1.6 (48%)	<b>0.6 Ga zircon:</b> +12/-25 (avg -1) <b>2.3-1.7 Ga zircon:</b> +6/-27 (avg -10)
Garzanti et al. 2013	Northern Arabia sand seas	LA-ICP-MS	1565/?	1.0-0.5 (74%), 1.1-1.0 (8%), 2.0-1.8 (3%), 2.6-2.5 (3%)	
Garzanti et al. 2017	Rub Al Khali, Saudi Arabia	LA-ICP-MS	3909/5454	1.10-0.49 (85%), 2.15-1.74 (5%), 2.73-2.40 (5%)	
This study	Sahara Desert	LA-ICP-MS	3996/5437	0.70-0.54 (51%), 1.1-0.9 (6%), 2.2-1.8 (11.7%) 2.70-2.47 (3%)	

**Declaration of interests**

The authors declare that they have no known competing financial interests or personal relationships that could have appeared to influence the work reported in this paper.

The authors declare the following financial interests/personal relationships which may be considered as potential competing interests:



# Provenance and recycling of Sahara Desert sand

Guido Pastore<sup>1</sup>, Thomas Baird<sup>2</sup>, Pieter Vermeesch<sup>2</sup>, Alberto Resentini<sup>1</sup>, Eduardo Garzanti<sup>1\*</sup>

<sup>1</sup>*Laboratory for Provenance Studies, Department of Earth and Environmental Sciences, University of Milano-Bicocca, 20126 Milano, Italy*

<sup>2</sup>*London Geochronology Centre, Department of Earth Sciences, University College London, London, WC1E 6BT, UK*

Email: [g.pastore2@campus.unimib.it](mailto:g.pastore2@campus.unimib.it) (Pastore), [thomas.baird.16@ucl.ac.uk](mailto:thomas.baird.16@ucl.ac.uk) (Baird), [p.vermeesch@ucl.ac.uk](mailto:p.vermeesch@ucl.ac.uk) (Vermeesch), [alberto.resentini@unimib.it](mailto:alberto.resentini@unimib.it) (Resentini), [eduardo.garzanti@unimib.it](mailto:eduardo.garzanti@unimib.it) (Garzanti),

\* Corresponding author

*Key words:* Sand petrography; Heavy minerals; U-Pb zircon ages; Multivariate statistics; Sedimentary processes; Recycling; Fluvial/eolian interactions; Wind-fed and river-fed sand seas; Pan-African Orogeny.

**ABSTRACT**

1  
2 We here present the first comprehensive provenance study of the Sahara Desert using a combination  
3  
4 of multiple provenance proxies and state-of-the-art statistical analysis. Our dataset comprises 44  
5  
6 aeolian-dune samples, collected across the region from 12°N (Nigeria) to 34°N (Tunisia) and from  
7  
8 33°E (Egypt) to 16°W (Mauritania) and characterised by bulk-petrography, heavy-mineral, and  
9  
10 detrital-zircon U–Pb geochronology analyses. A set of statistical tools including Multidimensional  
11  
12 Scaling, Correspondence Analysis, Individual Difference Scaling, and General Procrustes Analysis  
13  
14 was applied to discriminate among sample groups with the purpose to reveal meaningful  
15  
16 compositional patterns and infer sediment transport pathways on a geological scale. The overall  
17  
18 homogeneity across sand samples, however, precluded a detailed narrative.

19  
20 Saharan dune fields are, with a few local exceptions, composed of pure quartzose sand with very poor  
21  
22 heavy-mineral suites dominated by durable zircon, tourmaline, and rutile. Some feldspars, amphibole,  
23  
24 epidote, garnet, or staurolite occur closer to basement exposures, and carbonate grains, clinopyroxene  
25  
26 and olivine near a basaltic field in Libya. Relatively varied compositions also characterize sand along  
27  
28 the Nile Valley and the southern front of the Anti-Atlas fold belt in Morocco. Otherwise, from the  
29  
30 Sahel to the Mediterranean Sea and from the Nile River to the Atlantic Ocean, sand consists nearly  
31  
32 exclusively of quartz and durable minerals. These have been concentrated through multiple cycles of  
33  
34 erosion, deposition, and diagenesis of Phanerozoic siliciclastic rocks during the long period of relative  
35  
36 tectonic quiescence that followed the Neoproterozoic Pan-African orogeny, the last episode of major  
37  
38 crustal growth in the region. The principal ultimate source of recycled sand is held to be represented  
39  
40 by the thick blanket of quartz-rich sandstones that were deposited in the Cambro-Ordovician from  
41  
42 the newly formed Arabian-Nubian Shield in the east to Mauritania in the west. Durability of zircon  
43  
44 grains and their likelihood to be recycled from older sedimentary rocks argues against the assumption,  
45  
46 too often implicitly taken for granted in provenance studies based on detrital-zircon ages, that their  
47  
48 age distribution reflects transport pathways existing at the time of deposition rather than inheritance  
49  
50 from multiple and remote landscapes of the past.  
51  
52  
53  
54  
55  
56  
57  
58  
59  
60  
61  
62  
63  
64  
65



*“I have always loved the desert. You sit down on a sand dune. You see nothing. You hear nothing. And yet something shines, something sings in that silence.”*

Antoine de Saint-Exupéry, *The Little Prince*

## 1. Introduction

The Sahara is by far the largest hot desert on Earth, hosting several large dune fields. The provenance of these vast expanses of sand is gravely understudied. We here present the first thorough and comprehensive multidisciplinary study aimed at understanding the nature of sand sources, how sand evolved during geological time, and under the action of which prevailing wind regimes and along which trajectories was it displaced and eventually accumulated in the sand sea.

Our main purpose is to contribute to the ongoing debate in sedimentology and in Quaternary paleoclimatology concerning the production of sand and silt in arid landscapes. As far as quartzose sand is concerned (Dott, 2003; Muhs, 2004), one view is that sediment delivered from surrounding source rocks “matures” by essentially mechanical processes within the desert area (e.g., Dutta et al., 1993). Another is that the concentration of durable minerals is inherited from recycling of older sandstones that underwent extensive weathering in more aggressive climatic conditions, extensive intrastratal dissolution during diagenesis, or in general multiphase chemical leaching during multiple cycles of weathering and diagenesis (e.g., Garzanti, 2017).

Even more controversial are the generation mechanisms of “desert loess” (Smith et al., 2002; Lancaster, 2020). Throughout the Plio-Quaternary, the Sahara has represented a major source of fine particles, blown offshore to as far as the other side of the Atlantic Ocean (Muhs et al., 1990, 2019; Prospero, 1996) and is currently the largest source of mineral aerosols globally (Tegen et al., 2013).

Up to 85 megatonnes of dust are emitted into the atmosphere from the Sahara annually, with the Bodélé Depression representing the largest single area of dust production (Middleton and Goudie, 2001; Koren et al., 2006; Bakker et al., 2019). However, the precise mechanism behind the origin of mineral aerosol is hotly debated. Studies have suggested the predominant genesis for dust emissions

25 is the deflation of fine-grained sediments from depressed areas (e.g., [Bristow et al., 2009](#)), the  
26 abrasion of saltating sand grains within sand seas (e.g., [Crouvi et al., 2012](#)), or the accumulation of  
27 silt through hydrological factors, resulting in high emissions from alluvial deposits, desiccated lake  
28 beds, and palaeolakes ([Bakker et al., 2019](#); [Jewell et al., 2020](#)). The need to identify major sediment  
29 sources and clarify the process of sand and silt generation through tracing the main directions of  
30 aeolian transport within the Sahara are therefore much warranted.

31 This study investigates the origin, spatial variability, and transport pathways of aeolian sand in the  
32 Sahara by combining bulk-petrography, heavy-mineral, and detrital-zircon U–Pb geochronology  
33 analyses on 44 sediment samples. These samples have been collected in northern Africa across more  
34 than 20° degrees of latitude from the Sahel to the Mediterranean Sea and almost 50° degrees of  
35 longitude from the Nile River to the Atlantic Ocean ([Fig. 1](#)).

36 Highly detailed provenance studies of desert sand have been carried out with the same multitechnique  
37 approach in diverse sand seas of Africa, Arabia, and Asia (e.g., [Garzanti et al., 2012, 2017](#); [Stevens  
38 et al., 2013](#); [Rittner et al., 2016](#)) but not on the Sahara so far. Saharan dune sands have been broadly  
39 described as composed of quartz (e.g., [El-Baz, 1998](#); [Muhs, 2004](#); [Abdelhak et al., 2014](#); [Meftah and  
40 Mahboub, 2020](#)) but their provenance has remained unknown. To identify the source regions, gain  
41 understanding of sand transport pathways, and extract all possible provenance information from a  
42 composition characterized by only a limited number of provenance-diagnostic minerals, our study  
43 required the scrutiny of multi-proxy datasets using a full set of advanced statistical techniques.  
44 Multidimensional Scaling, Correspondence Analysis, Individual Difference Scaling, and General  
45 Procrustes Analysis were applied to provide both a highly robust statistical investigation and an  
46 unbiased visual representation of the relationships among the samples.

## 47 **2. Geomorphological framework**

### 48 *2.1. Climate and wind patterns*



52 The Sahara (in Arabic *sahra*, desert) covers an area of 9 million km<sup>2</sup> and extends from ~12°N to  
1  
53 ~34°N (Fig. 1). The desert thus straddles the Tropic of Cancer and is influenced by the descending  
3  
54 limb of the Hadley cell. The trajectory of air masses and rainfall are regulated by the strength of the  
4  
6  
55 subtropical high-pressure system and by the latitudinal shift of the Intertropical Convergence Zone  
8  
56 (ITCZ). Average annual precipitation is <50 mm in most areas, which may not see rain in many  
10  
11  
12  
57 consecutive years, and increases to ~160 mm in the semiarid Sahel to the south (from either the Arabic  
13  
14  
58 word *sahil*, shore, figurative for desert's edge, or *sahl*, plain).

16  
17  
59 During winter, the ITCZ shifts to the south and the Azores Anticyclone and the Sahara High are  
18  
19  
60 established, with only occasional disturbances by cyclonic systems from the Atlantic Ocean or by the  
20  
21  
61 polar front. Atmospheric circulation is dominated by westerly winds and by winds associated with  
22  
23  
24  
62 the Mediterranean depression, and the only maritime air masses enter the Sahara from the Red Sea.  
25  
26  
63 In the spring, the *khamseen* wind (in Arabic *khamseen*, fifty, because the wind blows over ~50 days)  
27  
28  
29  
64 moves hot tropical air towards the Mediterranean coast. In the summer, the northward displacement  
30  
31  
65 of the ITCZ allows air masses blown by recurved south-easterly trade winds to penetrate the  
32  
33  
34  
66 continent, and the West African Monsoon brings moisture to the southern Sahara. In its northern  
35  
36  
67 position, the ITCZ represents a barrier for air masses blown by the hot and dry north-easterly trade  
37  
38  
39  
68 winds (the *harmattan*; possibly derived indirectly from the Arabic word *haram*, evil), often regulated  
40  
41  
69 daily by the thermic inversion of near-surface air (Warner, 2009). Libya reaches one of the highest  
42  
43  
44  
70 temperatures on Earth (58°C) with extreme diurnal variation (up to 50°C), whereas lower  
45  
46  
71 temperatures are recorded in the northwest influenced by the incursion of cold air from the Atlantic  
47  
48  
72 Ocean.

50  
51  
73 A climatic zonation distinguishes the northern Sahara, affected by the winter Mediterranean  
52  
53  
74 depression, and the southern Sahara, characterized by the West African Monsoon in summer. This  
54  
55  
75 zonation is strengthened by the position of the main topographic highs (Hoggar, Tibesti, and Ennedi  
56  
57  
76 Mountains), hampering precipitations and southward sand transport from north to south (Wilson,  
58  
59  
60  
61  
62  
63  
64  
65

1971; Mainguet, 1978). Relief concentrates precipitation in summer and extreme events and flash floods occur when the monsoon pushes humid air against the Tibesti and Hoggar massifs.

Saharan sand-flow patterns are poorly constrained. Historically, the role of the subtropical high-pressure zone has been argued to split sand flows along a north-south divide (Wilson, 1971). In the northern zone, transport occurs mainly to the northeast, while the southern zone sees sand flow towards the coast of Mauritania and offshore into the Atlantic Ocean (Fig. 2). However, this theory relies on a short temporal sampling window and warrants revisiting.

## 2.2. Hydrology

Because of extreme aridity, river courses in the Sahara are transformed into desiccated dry valleys (in Arabic *wadi*, plural *widyan*), representing the remnants of the hydrological network inherited from wetter climatic stages in the past (Ghoneim et al., 2007; Abdelkareem and El-Baz, 2015; Abdelsalam, 2018). One example in the eastern Sahara is Wadi Howar (Fig. 1), sourced from the Ennedi and Darfur mountains and once draining northeastwards from the Chad/Sudan border to the Nile for 640 km but now marked only by linear tree vegetation sustained by the groundwater table in the shallow subsurface (Pachur and Kröpelin, 1987). The major exception is the Nile River (basin area ~3 million km<sup>2</sup>), which conveys across the desert the large volume of water received from East African lakes, augmented by monsoonal rains falling on the Ethiopian plateau in the summer (Sutcliffe and Parks, 1999).

The southeastern Sahara Desert receives water from the laterite-capped hilly plateau representing the water divide from the Congo and the source of several headwater branches of the Bahr El Ghazal, a western tributary of the Nile (in Arabic *bahr*, sea, figurative for big river). To the west, the Chari River and its major western Logone branch drain the Cameroon basaltic plateau to feed Lake Chad, a shallow body of water (depth mainly < 7 m) surrounded by seasonally inundated marshland (Fig. 1). Lake Chad is the only lake remaining in the desert, with a vast (2.5 million km<sup>2</sup>) endorheic drainage basin that receives monsoonal rain falling during summer in the south. Climate change and

104 increased water use for human activities make the lake vulnerable to drought events such as those of  
 105 the 1970s and 1980s, which saw the lake surface area shrink by up to 90% (Birkett, 2000; Coe and  
 106 Foley, 2001; Gao et al., 2011).

107 Farther west, the Niger River (basin area 2.3 million km<sup>2</sup>), sourced in the Guinea plateau only ~250  
 108 km from the Atlantic coast, draws a wide arc across the southern Sahara passing through an inland  
 109 delta in Mali and is eventually diverted southward towards the Gulf of Guinea (Gischler, 1976;  
 110 Goudie, 2005). The Atlas Mountains collect precipitation also in the form of snow, recharging the  
 111 large aquifers of the northwestern Sahara (Al-Gamal, 2011). In the eastern Sahara, subsurface water  
 112 is stored in Nubian sandstone aquifers across the political borders of Libya, Egypt, Sudan, and Chad  
 113 (Gossel et al., 2004).

### 115 2.3. Sand dunes

116 Sand dunes cover only a fifth of the immense surface of the Sahara. In order to understand the  
 117 relationships with wind regimes, dune forms and distribution have long been studied with field  
 118 expeditions (e.g., Bagnold, 1942; Capot-Rey, 1945) and satellite images (Breed et al., 1979;  
 119 Lancaster, 1995; El-Baz, 2000; Pye and Tsoar, 2008; Baird et al., 2019). Mainguet and Chemin (1983)  
 120 suggested that the central part of the desert, which is subjected to strong deflation, represents a major  
 121 source of sand for dune fields along its margins, where more humid climate, vegetation, and decreased  
 122 wind strength induce deposition especially close to the main topographic barriers.

123 In the western Sahara, linear dunes predominate from the coast inland, whereas crescentic dunes are  
 124 common to the south, associated with north-easterly anticyclonic circulation from the Sahara and  
 125 Azores high-pressure cells. In Mali and Niger, most dunes are partially vegetated under the influence  
 126 of monsoonal moisture. Two sets of dunes occur along the Niger River, one indicating northeastward  
 127 drift induced by trade winds, and the other oriented E/W with more spaced and eroded ridges.  
 128 Crescentic dunes and large isolated star dunes characterize the Erg de Bilma in Niger (Fig. 1;  
 129 Mainguet and Callot, 1978).



131 In the Moroccan desert close to the Atlantic coast, barchan dunes form under the effect of prevailing  
 132 winds from the northwest and moderate to low sand supply (Elbelrhiti, 2012). In the northern Sahara,  
 133 large sand seas with star dunes occupy depressions bordered by elevated areas. Star dunes are the  
 134 product of a complex, multi-directional wind regime (Lancaster, 1995; Zhang et al., 2012), resulting  
 135 from the interaction of winter westerlies with summer north-easterly and south-westerly winds  
 136 generated from cyclonic perturbations in Mediterranean and Atlantic depression systems. Star dunes  
 137 occur in the northern part of the Grand Erg Occidental, grading southward into crescentic dunes, and  
 138 are aligned in linear trends in the Grand Erg Oriental. A network of barchanoid dunes in southern  
 139 Tunisia is generated by high-energy winds, whereas crescentic or linear dunes grown in response to  
 140 unimodal or bimodal wind directions are more common south of 30°N (Breed et al., 1979).

#### 142 *2.4. Quaternary evolution*

143  
 144 Dry and wet climate alternated repeatedly in northern Africa during the Quaternary. Wind strength  
 145 fostering dune growth increased in the latest Pleistocene, followed by a humid early Holocene and  
 146 eventually by the return to arid conditions since the mid-Holocene. The desert expanded during the  
 147 Last Glacial Maximum, when the ITCZ was displaced towards the equator (Nicholson and Flohn,  
 148 1980; Arbuszewski et al. 2013) and dunes mobilized by stronger wind moved onto arid landscapes  
 149 (Grove and Warren, 1968; Swezey, 2001; Bristow and Armitage, 2016). Arid to humid transitions  
 150 seemingly occurred at 15-14.5 ka and 11.5-11 ka, in association with the reduction of polar ice-sheets,  
 151 strengthened hydrological circulation (Gasse, 2000), and northward displacement of the ITCZ (Haug  
 152 et al., 2001).

153 At the onset of the early Holocene African Humid Period (~14.5 ka), natural corridors opened to  
 154 allow the displacement of humans and other animals (Kuper and Kropelin, 2006; Drake et al., 2011).  
 155 The current aridity initiated between ~5.5 ka (deMenocal et al., 2000) and ~4.5 ka (Gasse, 2000), but  
 156 the timing and rate of desiccation that affected the Sahara and Sahel at the end of the African Humid

157 Period, including Mega-Lake Chad, remain controversial ([Sarnthein, 1978](#); [Bristow and Armitage,](#)  
158 [2016](#)).

159

### 160 **3. Geological framework**

161

162 Four partially overlapping geological domains can be identified in the Sahara Desert ([Fig. 3](#)): 1) the  
163 West African Craton, representing the oldest core of the continent; 2) the Tuareg Shield, including  
164 different sub-domains from east to west; 3) the Sahara Metacraton in the east, where the Archean  
165 cratonic core was intensely remobilized during the Pan-African orogeny; 4) Phanerozoic cover strata  
166 in the northern part of the desert, accumulated during multistep episodes of basin subsidence, tectonic  
167 inversion, and volcanic activity.

168

#### 169 *3.1. West African Craton*

170

171 The West African Craton comprises the Man Shield in the south and the Reguibat Shield in the north.  
172 These terranes include an Archean core, built during the Leonian (3.0-2.9 Ga) and Liberian (2.7-2.6  
173 Ga) orogenic cycles ([Feybesse and Milési, 1994](#)), bordered by Proterozoic to Phanerozoic mobile  
174 belts and sedimentary basins. The eastern Reguibat Shield and the Man Shield were affected by the  
175 Eburnean orogeny (~2.0 Ga), when the high-grade Birimian basement formed ([Abouchami et al.,](#)  
176 [1990](#)). The Anti-Atlas Mountains in Morocco also contain Paleoproterozoic basement, including  
177 granites as well as metasedimentary and metavolcanic rocks ([Thomas et al., 2002](#)).

178

179 During the Pan-African orogeny (0.85-0.55 Ga), one of the most extensive mountain-building events  
180 of the Earth's history that assembled the Arabian-Nubian Shield and deeply affected the Sahara  
181 Metacraton, the 3000 km-long Trans-Sahara belt formed as a result of collisions among the West  
182 African Craton, the Congo Craton, and the Sahara Metacraton. High sediment influx caused the filling  
183 of the Taoudeni (in the south) and Tindouf (in the north) intraplate basins ([Fig. 3](#); [Nance et al., 2008](#)).

184

185 Low-grade metamorphism and granite intrusions took place along the margins of the West African  
186 Craton ([Black et al., 1979](#)), whereas volcanic sequences and transpressional deformation are

187

188

189

185 documented in the Anti-Atlas to the north (Ennih and Liégeois, 2001). In the east, the Pan-African  
 186 event is responsible for the formation of thrust belts along the western side of the West Africa Craton  
 187 (Villeneuve, 2008), which developed only minor tectonic structures in the foreland of the Paleozoic  
 188 Variscan orogeny (Ennih and Liégeois, 2008). The Cenozoic Alpine orogeny affected only the  
 189 northernmost part of the African continent forming the High Atlas of Morocco (Mattauer et al., 1977).

### 191 3.2. Tuareg Shield

192 The Tuareg Shield, located between the West African Craton in the west and the Sahara Metacraton  
 193 in the east, developed during the Neoproterozoic by eastward subduction and closure of the Aoujej  
 194 and Imira oceanic realms at 700 and 625 Ma, and consequent accretion of different terranes (Caby et  
 195 al. 1981, 1989; Fabre et al., 1982). High-temperature N/S shear zones were interpreted to document  
 196 post-collisional lateral escape of rigid tectonic blocks (Liégeois, 2019).

197 During the Pan-African orogeny, granulitic gneisses of Archean and Paleoproterozoic age in the  
 198 central Hoggar (e.g., Unité Granulitique de Iforas) were remobilized with development of  
 199 amphibolite-facies mega-shear zones (Liégeois et al., 1994) and the Tuareg Shield was heavily  
 200 reworked (Bertrand and Caby, 1978). To the southwest, the Adrar des Iforas Massif recorded several  
 201 magmatic events, including emplacement of the Renatt leucogranite (Liégeois et al., 1994),  
 202 continental-arc andesites (Chikhaoui et al., 1978), alkaline plutons between 600 and 580 Ma (Fezaa  
 203 et al., 2019), as well as late/post orogenic plutons, dykes, and volcanic rocks between 570 and 520  
 204 Ma (Liégeois and Black, 1987).

205 The Air Mountains in the southwestern Tuareg Shield include three N/S elongated terranes  
 206 (Aouzegueur, Barghot, and Assodé) containing high-grade metasedimentary rocks and serpentinites  
 207 (Boullier et al., 1991; Moreau et al., 1994). Granites cross-cutting the main deformation were intruded  
 208 at  $664 \pm 8$  Ma in the Barghot domain and between 645 and 580 Ma in the Assodé domain (Liégeois et  
 209 al., 1994). The Aouzegueur and Barghot terranes were thrust eastward over the Saharan Metacraton  
 210 in the late Neoproterozoic (Liégeois et al., 2000). A ring complex including anorthosite was emplaced



212 in the Aïr Mountains during the early Devonian (Black, 1965), whereas Cenozoic magmatism was  
 1 volumetrically negligible.

214 The northeastern border of the Tuareg Shield was affected by a major intracontinental tectono-  
 6 magmatic event at 575–555 Ma, associated with the indentation of the cratonic basement of the  
 8 Murzuq Basin (Fezaa et al., 2010).

### 217 3.3. Sahara Metacraton

219 The Saharan Metacraton (Fig. 3), separated by a mega-shear from the Tuareg Shield in the west and  
 17 from the Arabian-Nubian Shield in the east, consists of Archean and Paleoproterozoic continental  
 19 crust profoundly remobilized during the Pan-African orogeny, when migmatitic gneisses and  
 22 metasedimentary rocks were intruded by granitoids between 750 and 550 Ma (Abdelsalam et al.,  
 24 2002). Various geodynamic processes, including continental collision (Schandelmeier et al., 1988),  
 25 delamination of subcontinental mantle (Bird, 1979), lithospheric extension (Denkler et al., 1994), and  
 27 assemblage of exotic terranes (Rogers et al., 1978) have been invoked to explain the Neoproterozoic  
 29 evolution of the metacraton (Ghuma and Rogers, 1978; Pinna et al., 1994). In the east, an ophiolitic  
 32 suture contains low-grade volcanoclastic rocks possibly documenting the closure of a failed rift (Stern  
 34 et al., 1994; Kuster and Liegeois, 2001).

### 31 3.4. Phanerozoic sedimentary and volcanic rocks

33 The northern part of the Sahara is largely covered by Paleozoic to Cenozoic rocks deposited in  
 45 sedimentary basins formed in the wake of the Pan-African orogeny and subsequently by extensional  
 47 reactivation of inherited tectonic structures (Echikh, 1998; Bumby and Giraud, 2005).

36 Between the mid-Cambrian and the Late Ordovician (520–440 Ma), quartz-rich sandstones were  
 52 deposited all across northern Africa, possibly as a continuous blanket from Oman in eastern Arabia  
 53 to Mauritania with an average thickness of ~1 km and a volume of ~10 million km<sup>3</sup> (Burke, 1999).

39 Their deposition followed the Pan-African orogeny and post-Pan-African continental wrenching, and  
 60 characterized the ensuing phase of cooling and thermal subsidence that generated the accommodation

241 space for the widespread accumulation of sand sheets. At that time, quartz-rich sandstones were  
 1  
 242 deposited also in other parts of Gondwana and even in North America (e.g., St. Peter Sandstone; [Dott,](#)  
 3  
 243 [2003](#)). Quartz-rich composition is highly unusual for orogenic detritus ([Dickinson, 1985](#); [Garzanti et](#)  
 4  
 244 [al., 2007](#)), an anomaly that still needs understanding. If these sediments are indeed first cycle, then  
 6  
 245 *ad hoc* explanations are required. Cambro-Ordovician landscapes still devoid of vegetation and  
 8  
 246 supposedly characterized by low relief and low sedimentation rates are envisaged to have suffered  
 10  
 247 very extensive chemical weathering, fostered by warm humid climate and by an unusually corrosive  
 11  
 248 atmosphere following late Neoproterozoic volcanism ([Burke, 1999](#); [Avigad et al., 2005](#)). This  
 13  
 249 scenario is apparently at odds with the major glaciation that affected Gondwana in the Late  
 14  
 250 Ordovician, which itself represents a geological paradox, having occurred within a long greenhouse  
 15  
 251 period with high atmospheric CO<sub>2</sub> levels ([Brenchley et al., 1994](#); [Ghienne et al., 2014](#)).

252 In the Silurian, tectonic subsidence favoured the accumulation of marine to lacustrine sediments,  
 26  
 253 overlain by shallow-marine clastics in the Murzuq Basin of Libya, in western Algeria, and in southern  
 27  
 254 Morocco ([Fekirine and Abdallah, 1998](#)). Failed rifts were inverted during the Carboniferous as a  
 28  
 255 consequence of Variscan convergence, affecting mostly Morocco and less intensely Algeria and  
 29  
 256 Libya ([Haddoum et al., 2001](#)). The High Atlas graben system formed in the Triassic and Jurassic  
 30  
 257 extending eastwards to northeastern Algeria and Tunisia ([Coward and Ries, 2003](#)). During the  
 31  
 258 Cretaceous, the Sirte Basin developed as another horst-and-graben system filled by shale and  
 32  
 259 evaporite ([Thusu and Mansouri, 1995](#)). In the northern Murzuq Basin, these strata are overlain by  
 33  
 260 basaltic lavas of the Haruj al Aswad Massif, emplaced in multiple phases between 4 and 0.5 Ma and  
 34  
 261 triggered by reactivation of Tibesti-Sirte basement faults ([Cvetković et al., 2010](#); [Elshaafi and](#)  
 35  
 262 [Gudmundsson, 2016](#)).

#### 264 4. Sampling and methods

265  
 266 In this study, we analysed an archive of 45 sand samples of aeolian dunes, 36 collected between 2003  
 267 and 2019 by different operators across the Sahara Desert: 4 from Chad; 5 from Lake Chad, northern

268 Nigeria, and southern Niger; 8 from central Niger; 1 from Burkina Faso; 2 from Mali; 4 from  
 1  
 269 Mauritania; 3 from Morocco; 3 from Algeria; 2 from Tunisia; 3 from Libya; and 1 from western  
 3  
 270 Egypt. Data are also provided for 9 additional aeolian dunes from Egypt: 3 from the Western Desert  
 4  
 5  
 6  
 271 and 6 from the Nile Valley to the west of the Nile River. Aeolian dunes to the east of the Nile River  
 8  
 272 containing Nile-derived volcanic detritus (Muhs et al., 2013; Garzanti et al., 2015a) were considered  
 9  
 10  
 11  
 273 as separated from the rest of the Sahara and thus not included in this study. GPS coordinates and  
 13  
 14  
 274 further information on all sampling sites are provided in Appendix Table A1 and Google Earth™ file  
 15  
 16  
 275 Sahara.kmz.

#### 18 19 20 21 4.1. Petrography

22  
 23  
 24 Bulk sand samples were impregnated with araldite epoxy, cut into standard thin sections, and  
 25  
 26 analysed by counting 450-500 points under the petrographic microscope (Gazzi-Dickinson method;  
 27  
 28 Ingersoll et al., 1984). Sand classification was based on the relative abundance of the three main  
 29  
 30  
 31 framework components quartz (Q), feldspars (F), and lithic fragments (L), considered if exceeding  
 32  
 33 10%QFL. According to standard use, the less abundant component goes first, the more abundant last  
 34  
 35  
 36 (e.g., a sand is named litho-quartzose if  $Q > L > 10\%QFL > F$ ). Feldspar-rich feldspatho-quartzose  
 37  
 38 ( $1 < Q/F < 2$ ), feldspatho-quartzose ( $2 < Q/F < 4$ ), quartz-rich feldspatho-quartzose ( $4 < Q/F < 9$ ),  
 39  
 40  
 41 quartzose ( $90\% < Q/QFL < 95\%$ ), and pure quartzose compositions ( $Q/QFL > 95\%$ ) are distinguished  
 42  
 43 (classification scheme after Garzanti, 2019). These distinctions are essential to discriminate among  
 44  
 45  
 46 quartz-rich suites generated in anorogenic settings (Garzanti et al., 2001, 2018a). Metamorphic rock  
 47  
 48 fragments were subdivided into very low to low-rank metasedimentary or metavolcanic, and medium  
 49  
 50  
 51 to high-rank felsic or mafic categories (Garzanti and Vezzoli, 2003). The intrabasinal *versus*  
 52  
 53  
 54 extrabasinal origin of carbonate and non-carbonate grains was established based on criteria illustrated  
 55  
 56  
 57 in Zuffa (1985) and Garzanti (1991). Petrographic parameters used in this article include the  
 58  
 59  
 60 plagioclase/total feldspar (P/F) ratio; feldspar identified by cross-hatch twinning is called microcline\*  
 61  
 62  
 63 through the text. Median grain size was determined in thin section by ranking and visual comparison  
 64  
 65



with in-house standards composed of mounts of sieved  $\Phi/4$  classes. Key petrographic parameters are provided in [Table 1](#) and the complete petrographic dataset in [Appendix Table A2](#).

#### 4.2. Heavy minerals

From a split aliquot of each sample of well sorted aeolian sand, the dense fraction was separated by centrifuging in Na-metatungstate (density  $2.90 \text{ g/cm}^3$ ) and recovered by partial freezing with liquid nitrogen (method described in detail in [Andò, 2020](#)). Samples were analysed in bulk to obtain a faithful characterization of the entire heavy-mineral suite. In order to determine correct volume percentages,  $\geq 200$  transparent heavy minerals were point-counted at suitable regular spacing on each grain mount ([Garzanti and Andò, 2019](#)). In previous analyses of 9 Egyptian samples, different size fractions were used ( $> 95$  or  $95\text{-}500 \mu\text{m}$  for Western Desert samples and  $63\text{-}250 \mu\text{m}$  for Nile Valley samples) and heavy minerals were counted by the area method ([Galehouse, 1971](#)).

Transparent heavy-mineral assemblages, called for brevity “tHM suites” throughout the text, are defined as the spectrum of detrital extrabasinal minerals with density  $>2.90 \text{ g/cm}^3$  identifiable under a transmitted-light microscope. Rock fragments, iron oxides, soil clasts, phyllosilicates, and carbonates were not considered as integral part of the tHM suite. According to the concentration of transparent heavy minerals (tHMC), tHM suites are described as “extremely poor” ( $\text{tHMC} < 0.1$ ), “very poor” ( $0.1 \leq \text{tHMC} < 0.5$ ), “poor” ( $0.5 \leq \text{tHMC} < 1$ ), and “moderately poor” ( $1 \leq \text{tHMC} < 2$ ). The ZTR index (sum of zircon, tourmaline and rutile over total tHM; [Hubert 1962](#)) expresses the durability of the tHM suite. Significant detrital components are listed in order of abundance (high to low) throughout the text. Key heavy-mineral parameters are provided in [Table 1](#) and the complete dataset in [Appendix Table A3](#).

#### 4.3. Detrital geochronology

Detrital zircons were identified by Automated Phase Mapping ([Vermeesch et al., 2017](#)) with a Renishaw inVia<sup>TM</sup> Raman microscope on the heavy-mineral separates of 32 selected samples,

323 concentrated with standard magnetic techniques and directly mounted in epoxy resin without any  
 1  
 324 operator selection *via* hand picking. U-Pb zircon ages were determined at the London Geochronology  
 3  
 325 Centre using an Agilent 7900 LA-ICP-MS (laser ablation-inductively coupled plasma-mass  
 4  
 5  
 6  
 326 spectrometry) system, employing a NewWave NWR193 Excimer Laser operated at 10 Hz with a 25  
 8  
 9  
 327  $\mu\text{m}$  spot size and  $\sim 2.5 \text{ J/cm}^2$  fluence. No cathodo-luminescence imaging was conducted, and the laser  
 10  
 11  
 328 spot was always placed “blindly” in the middle of zircon grains in order to treat all samples equally  
 13  
 14  
 329 and avoid bias in intersample comparison (“blind-dating approach”, illustrated and discussed in  
 15  
 16  
 330 [Garzanti et al., 2018b](#)). Many samples were subsequently analysed targeting zircon rims and nearly  
 18  
 19  
 331 identical results were obtained. No common Pb correction was applied. The mass spectrometer data  
 20  
 21  
 332 were converted to isotopic ratios using GLITTER 4.4.2 software ([Griffin et al., 2008](#)), employing  
 23  
 24  
 333 Plešovice zircon ([Sláma et al., 2008](#)) as a primary age standard and GJ-1 ([Jackson et al., 2004](#)) as a  
 25  
 26  
 334 secondary age standard. A NIST SRM612 glass was used as a compositional standard for U and Th  
 28  
 29  
 335 concentrations. GLITTER files were post-processed in R using IsoplotR 2.5 ([Vermeesch, 2018a](#)). We  
 30  
 31  
 336 used  $^{206}\text{Pb}/^{238}\text{U}$  and  $^{207}\text{Pb}/^{206}\text{Pb}$  as preferred ages for zircons younger and older than 1100 Ma,  
 33  
 34  
 337 respectively. We calculated concordia ages as the maximum likelihood intersection between the  
 35  
 36  
 338 concordia line and the error ellipse of  $^{207}\text{Pb}/^{235}\text{U}$  and  $^{206}\text{Pb}/^{238}\text{U}$  ages ([Ludwig, 1998](#); [Vermeesch,](#)  
 37  
 38  
 339 [2021](#)); ages with  $> -5/+15\%$  relative discordance were considered discordant. The concordia ages were  
 40  
 41  
 340 used for statistical analysis. The complete geochronological dataset, comprising  $\sim 4000$  concordant  
 42  
 43  
 341 ages ( $> 100$  ages on 26 samples) is provided in [Appendix B](#).  
 44  
 45

#### 342 4.4. Statistical tools

343  
 344  
 345 Multidimensional Scaling (MDS; [Kruskal and Wish, 1978](#); [Vermeesch, 2013](#)) is a multivariate  
 50  
 51  
 52  
 346 ordination technique that takes a dissimilarity matrix as input and produces a map of samples as  
 54  
 55  
 347 output, in which similar samples plot close together and dissimilar samples plot far apart. For detrital  
 56  
 57  
 348 zircon U-Pb age spectra, a dissimilarity matrix can be constructed using the Kolmogorov-Smirnov  
 58  
 59  
 349 statistic (i.e., the maximum vertical difference between two cumulative distribution functions; [Feller,](#)  
 61  
 62  
 63  
 64  
 65

350 [1948](#)). Correspondence Analysis (CA) is an ordination technique that is specifically tailored for count  
1  
351 data such as petrographic and heavy-mineral point counts ([Greenacre, 2017](#)). This method can be  
3  
352 shown to be a special case of MDS in which the dissimilarity matrix is populated with chi-square  
4  
5  
6  
353 distances ([Vermeesch, 2018b](#)).

354 General Procrustes Analysis (GPA) and Individual Difference Scaling (INDSCAL) are higher-order  
9  
10  
11  
355 data-mining techniques that combine several MDS maps together in order to simplify the  
12  
13  
356 interpretation of ‘big’ datasets ([Vermeesch and Garzanti, 2015](#)). In the case of GPA, this is achieved  
14  
15  
16  
357 by mapping the different MDS configurations onto a common configuration by a number of affine  
17  
18  
19  
358 transformations (reflection, rotation, scaling, and translation; [Gower, 1975](#)). INDSCAL, on the other  
20  
21  
22  
359 hand, acts directly on the dissimilarity matrices. It is a higher order generalisation of the MDS method  
23  
24  
360 that aims to fit multiple dissimilarity matrices to a shared ‘group configuration’ by attaching different  
25  
26  
361 weights to the different datasets ([Carroll and Chang, 1970](#)).

362 Dissimilarity matrices for the different provenance proxies for multivariate ordination were also used  
28  
29  
30  
363 to construct hierarchical clustering dendrograms with the normalised distance values obtained by chi-  
31  
32  
33  
364 squared distance (for CA) and Kolmogorov-Smirnov distance (for MDS). Thus we were able to assign  
34  
35  
365 the samples to different clusters, thereby augmenting further the visual interpretation ([Fig. 8A,B,C](#)).  
36  
37  
366 The same method was applied to the GPA matrices of dissimilarities displayed in [Fig. 8E,F](#).  
38  
39  
40  
367 Additional statistical tools are presented in [Appendix C](#).  
41  
42

43  
368 To illustrate heavy-mineral data we used the compositional biplot ([Gabriel, 1971](#); [Greenacre, 2017](#)),  
44  
45  
369 a statistical/graphical display that allows discrimination among multivariate observations (points)  
46  
47  
370 while shedding light on the mutual relationships among multiple variables (rays). The length of each  
48  
49  
50  
371 ray is proportional to the variance of the corresponding variable in the dataset. If the angle between  
51  
52  
372 two rays is close to 0°, 90° or 180°, then the corresponding variables are directly correlated,  
53  
54  
55  
373 uncorrelated, or inversely correlated, respectively.  
56  
57

## 374 375 **5. Results**

61  
62  
63  
64  
65



376

377 In this section we shall first summarize the general petrographic, heavy-mineral, and detrital-  
 378 geochronology signatures of Saharan dune sands. Next, we shall highlight the characteristic  
 379 compositional features of each region (Fig. 4).

380

### 381 *5.1. Overview of detrital signatures*

382

383 Most analysed sand samples (33 out of 44) are pure quartzose (Fig. 5), including all of those from the  
 384 southeastern Sahara. In pure quartzose sands, orthoclase generally prevails over plagioclase and  
 385 microcline\*. The sum of lithic grains, micas and heavy minerals is <2% of total framework grains.  
 386 The tHM suites of most samples (35 out of 44) are very poor to extremely poor and characterized by  
 387 durable minerals (ZTR 25-96, anticorrelating with tHMC:  $r = 0.62$ , sign.lev. 0.1%) (Fig. 6). Zircon is  
 388 most common, followed by tourmaline, epidote, amphibole, rutile, clinopyroxene, garnet, and  
 389 staurolite.

390 Detrital zircon in Saharan dunes invariably yielded dominant Pan-African (Ordovician-  
 391 Neoproterozoic) U-Pb ages, with a virtually continuous distribution between 0.48 and 1.1 Ga (77%  
 392 of total ages), a prominent Cambrian-Ediacaran peak (0.5-0.6 Ga), a minor peak around 1.0 Ga, and  
 393 an intervening broader cluster in the Cryogenian (0.65-0.8 Ga) (Fig. 7). Younger ages are Paleozoic  
 394 (1.6%), Mesozoic (0.5%) and Cenozoic (0.2%). Older ages cluster between 1.8 and 2.2 Ga (11.7%)  
 395 and between 2.47 and 2.7 Ga (2.8%). Zircon grains dated between 1.1 and 1.8 Ga and between 2.2  
 396 and 2.47 Ga represent 3.4% and 1.2% of total ages, respectively, whereas those older than 2.7 Ga  
 397 represent 1.6%, with single ages as old as ~4 Ga.

398

### 399 *5.2. The southern Sahara*

400

401 All across the southern Sahara, from Chad to the Atlantic Ocean, dune sand displays rather  
 402 monotonous detrital signatures (Table 1). Both around the Bodélé Depression and in the Lake Chad  
 403 region sand is pure quartzose with high ZTR indices (Fig. 4F, 4I). Minor K-feldspar occurs (sample

404

405

406

407

408

409

404 5609) and minor staurolite characterizes the Lake Chad region. Sample 5607 from Nigeria displays  
 1  
 405 a sharp Ediacaran peak (44% of zircon grains).

406 In the ergs of central Niger, dune sand is pure quartzose with dominant durable minerals, locally  
 4 associated with minor garnet or pyroxene (sample 3235). Closer to the eastern side of the Aïr  
 6  
 407 Mountains, some grains of K-feldspar or plagioclase occur and tHM suites locally include common  
 8  
 408 amphibole, epidote, and staurolite. Orosirian zircon ages are slightly more common in this region and  
 10  
 409 Cambrian ages are also observed (3232) as well as one grain as young as 6 Ma (3233). On the western  
 12  
 410 side of the Aïr Mountains, sand is feldspatho-quartzose with significant polycrystalline quartz,  
 14  
 411 orthoclase, microcline\*, and sericitized plagioclase (Fig. 4H). The tHM suite is dominated by  
 16  
 412 amphibole (mostly blue-green hornblende) associated with zircon and epidote. The zircon-age  
 18  
 413 spectrum is also distinct, characterized by a sharp Ediacaran peak (47% of total ages), by secondary  
 20  
 414 Orosirian (24%) and Silurian-Mississippian clusters (320-435 Ma; 19%), and by lack of ages older  
 22  
 415 than the Orosirian.

416  
 30  
 417 Pure quartzose sand contains different amounts of ZTR minerals in Burkina Faso south of the Niger  
 32  
 33  
 418 River (common epidote), Mali, and Mauritania (locally common epidote or pyroxene with minor  
 35  
 419 garnet, staurolite, and amphibole) (Fig. 4D,G). Amphibole increases close to the Atlantic coast. Sand  
 37  
 420 collected in Burkina Faso yielded a minor cluster of Early-Middle Jurassic detrital-zircon ages (4%  
 38  
 421 of total grains). Zircon grains in Mali and Mauritania yielded a significant number of Orosirian (7-  
 40  
 422 13% of total grains), Rhyacian (7-12%) and Archean ages (3-10%), and only minor Tonian (2-5%)  
 42  
 423 and Stenian ages ( $\leq 4\%$ ).

### 424 425 *5.3. The northern Sahara*

426  
 52  
 427 In the northern Sahara, sand composition is more varied. Sand collected along the southern and  
 54  
 428 eastern front of the Anti-Atlas Mountains in Morocco ranges from pure quartzose to litho-quartzose  
 56  
 429 with granitoid, mafic volcanic, sedimentary, or very-low-rank to medium-rank metasedimentary rock  
 58  
 430 fragments (Fig. 4A). The tHM suite includes clinopyroxene associated with epidote, pumpellyite,  
 60  
 61  
 62  
 63  
 64  
 65

prehnite, amphibole, and durable ZTR minerals. The obtained zircon ages are mostly Neoproterozoic and Orosirian, with one grain as young as 5 Ma (sample 3269).

Dune sand in the Grand Erg Occidental in Algeria is pure quartzose with dominant durable minerals, whereas dune sand of the Grand Erg Oriental in Algeria and Tunisia is quartzose (Fig. 4E), with K-feldspar including microcline\* predominating over plagioclase, and locally dominant garnet (5616) or common amphibole and epidote (Table 1). Zircon grains yielded more Ediacaran ages in the Grand Erg Occidental and more Stenian ages in the Gran Erg Oriental.

In the Ubari Erg of Libya, dune sand is pure quartzose with dominant durable minerals associated with mainly actinolitic amphibole and epidote in the east. Dune sand collected in the Murzuq Erg near the Haruj al Aswad volcanic field (5584), instead, is litho-quartzose carbonaticlastic with a moderately poor tHM suite dominated by clinopyroxene and olivine (Fig. 4C). Orosirian ages of detrital zircon decrease, and Archean ages increase, from west to east across the Libyan desert.

In pure quartzose sand of the Western Desert in Egypt, durable minerals are associated with epidote, garnet, and minor hornblende, staurolite and clinopyroxene. The zircon-age spectrum of sample 5601 in the northwest is similar to those of Libyan sands.

Detrital modes are varied in dune sand collected along the western side of the Nile Valley. In the Aswan area, litho-quartzose carbonaticlastic to quartzose sand contains a moderately poor tHM suite with epidote, amphibole, and clinopyroxene. Dune sand to the north ranges from quartz-rich feldspatho-quartzose, with K-feldspar including microcline\* predominating over plagioclase, to litho-quartzose sedimentaclastic, quartzose, and pure quartzose. The very poor to moderately poor tHM suites include durable ZTR minerals associated with epidote, staurolite, hornblende, garnet, locally clinopyroxene, and minor kyanite (Table 1).

## 6. Data analysis

All compositional datasets (petrography, heavy minerals, detrital-zircon geochronology) are remarkably homogeneous, indicating that most Sahara dune sands are either derived from similar



458 sources or have been homogenized through multiple sedimentary cycles. Notable differences in  
1  
459 compositional signals do occur, but only related to the local addition of volcanic, orogenic, or  
3  
460 different sedimentary detritus (Fig. 4). Otherwise, identifying specific provenances, tracing sediment  
4  
6  
461 dispersal, and linking transport pathways with prevailing patterns of atmospheric circulation and wind  
8  
9  
462 regimes represents an arduous task. After this visual inspection of the data, we now turn to the  
10  
11  
463 multivariate ordination techniques to further investigate our results, in the anticipation that these tools  
13  
14  
464 may be able to detect hidden patterns and trends that the naked eye might have missed (Fig. 8).  
15  
16

### 465 466 *6.1. Petrographic dataset*

467  
468 Correspondence Analysis of petrographic data (Fig. 8A) highlights the very limited variability of  
22  
23  
469 quartz content, with dominance of pure quartzose sand across the Sahara (Table 1). A significant  
24  
25  
470 variability is observed for K-feldspar and plagioclase, which show a correlated behaviour. Quartz-  
27  
28  
471 rich feldspatho-quartzose samples from the western Aïr mountains, Grand Erg Oriental, and Nile  
29  
30  
472 Valley have low P/F ratio (24-29%) and low tHMC index, suggesting recycling of locally exposed  
32  
33  
473 sandstones ultimately derived from basement rocks rather than first-cycle supply from crystalline  
34  
35  
474 basement. Siltstone and metamorphic lithic grains are more common along the front of the Anti-Atlas  
36  
37  
475 in Morocco, reflecting orogenic contributions. Nile Valley and Murzuq Basin sands are enriched in  
39  
40  
476 carbonate grains derived from Cenozoic cover strata of the Sahara Metacraton.  
41  
42

### 477 478 *6.2. Heavy-mineral dataset*

479  
480 Correspondence Analysis of heavy-mineral data (Fig. 8B) highlights the anti-correlation between  
48  
49  
481 durable ZTR minerals and epidote + garnet + amphibole, the triad forming the mineralogical suite  
50  
51  
482 typical of metamorphic basements (Garzanti and Andò, 2007). The variability of the ZTR index  
53  
54  
483 matches that of quartz, indicating a concordant behaviour of all durable minerals typical of  
55  
56  
484 extensively recycled sediments. Epidote, amphibole and garnet are correlated (Fig. 6) and relatively  
58  
59  
485 common both west and east of the Aïr Mountains, in the Western Desert of Egypt and along the Nile  
60  
61  
62  
63  
64  
65

486 Valley, with maxima reached in coastal Mauritania and in the Grand Erg Oriental in Algeria. Sample  
1  
487 5616 is the only garnet-dominated sand. Clinopyroxene content varies widely, being most abundant  
3  
488 in the NE Murzuq sample 5584, where it is associated with olivine (Fig. 4C), and in all three  
4  
5  
6  
489 Moroccan samples also containing prehnite and pumpellyite (Table 1).  
8  
9

### 490 6.3. Detrital-zircon age dataset

491  
492 Besides KDE plots — which basically highlight the ubiquitous Pan-African peak with lesser  
12  
13  
493 “Grenvillian” (~1 Ga) and “Eburnean” (~2 Ga) clusters (Fig. 7) thus underscoring the homogeneity  
15  
494 of geochronological signatures across the Sahara —, the MDS map allows us to extract additional  
17  
18  
495 information from zircon-age distributions (Fig. 8C). Geographically closer samples tend to plot closer  
19  
20  
496 to each other, as in Chad and Mauritania. Hierarchical clustering analysis (Fig. C3 in Appendix C)  
22  
23  
497 points to a systematic difference between southeastern Sahara samples, characterized by a more  
24  
25  
498 prominent ~1.0 Ga peak, and northwestern Sahara samples, yielding fewer Stenian zircons and  
27  
28  
499 characterized by a larger Paleoproterozoic peak and some Paleozoic and Mesozoic ages. Sample 5610  
29  
30  
500 from west of the Aïr Mountains is singled out by the presence of a Paleozoic peak and the virtual lack  
31  
32  
501 of ~1.0 Ga grains.  
34  
35  
502

### 503 6.4. Inferences based on combined datasets

504  
505 Statistical analysis of single datasets meets only limited success in the attempt to highlight significant  
42  
43  
506 regional differences among the remarkably homogeneous provenance signatures of Sahara Desert  
44  
45  
507 sand. Within each dataset, dissimilarities are mostly small only excepting the few samples  
46  
48  
508 documenting additional sediment contribution from local sources. In such a case of homogeneous  
49  
50  
509 data, statistical analysis may easily emphasize minor local anomalies and overstress their  
51  
510 significance. Combining framework-petrography, heavy-mineral, and geochronological datasets with  
53  
54  
511 multivariate analysis produces visual plots (Fig. 8D, 8F) that help us not only to increase  
55  
56  
512

513 discrimination power but also to verify the consistency of potential artefacts, thus leading to more  
1  
514 robust results.

515 The INDSCAL plot (Fig. 8D) shows that three quarters of our samples have the same petrographic  
4  
516 and heavy-mineral fingerprint, preventing any provenance discrimination among them. These  
6  
517 samples are widely distributed from Chad to Tunisia and from the Western Desert of Egypt to  
8  
518 Mauritania, thus failing to display a definite geographical distribution across the Sahara. Some  
10  
519 significant differences are however confirmed, concerning samples collected along the Nile Valley  
12  
520 in Egypt and the Anti-Atlas front in Morocco, or in the NE Murzuq Erg (5584) and the Aïr Mountains  
14  
521 in western Niger (5610). Sample 5616 from Algeria is singled out by its garnet-dominated tHM suite.  
16  
20

21  
522 In the GPA plot (Fig. 8F), clusters were based on the hierarchical clustering dendrogram (Fig. 8E),  
23  
523 but addition of detrital-zircon ages does not change the overall picture substantially, maintaining the  
25  
524 difference between NW Sahara and SE Sahara samples documented by MDS analysis of the zircon-  
26  
525 age dataset. The distinctive local provenance of samples collected along the Anti-Atlas front in  
28  
526 Morocco (3269), in the Grand Erg Oriental (5616), in the NE Murzuq Erg (5584), and west of the  
30  
527 Aïr Mountains (5610) is confirmed. Other samples from Tunisia (5611), Mauritania (5600), and Chad  
32  
528 (5602) have no peculiar petrographic or heavy-mineral fingerprint and they are singled out mainly by  
34  
529 subtle differences in their zircon-age spectra (further statistical analysis is presented in Appendix C).  
36  
40  
530 This is thus considered either of local significance or as one case of artefact produced by the statistical  
42  
531 algorithm (i.e., a false positive) which, in the search of a signal, ends up emphasizing noise.  
44

45  
532 Even a thorough analysis conducted with sophisticated statistical techniques including  
47  
533 Multidimensional scaling (MDS), Correspondence analysis (CA), Individual Difference Scaling  
49  
534 (INDSCAL), and General Procrustes Analysis (GPA), therefore, could not break the compositional  
51  
535 homogeneity of Sahara dune sands. Rather, the power of these techniques to reveal even the most  
53  
536 subtle trend in a large dataset carries the risk of producing spurious results caused by local factors  
55  
537 such as wind sorting or bias in sampling or analytical procedures.  
57  
59

60  
538

### 539 6.5. Local sediment sources

540  
541 Petrographic, heavy-mineral, and geochronological signatures and their remarkable homogeneity  
542 indicate that Saharan sands have an overwhelmingly multicyclic origin, as discussed in detail in  
543 [section 7](#) below. Among the few differences highlighted by statistical analysis ([Fig. 8](#)), the two  
544 samples consistently displaying a distinct compositional fingerprint are those from the northeastern  
545 Murzuq basin (5584) and western Niger (5610).

546 The NE Murzuq sample is the richest in limestone grains, transparent heavy minerals, clinopyroxene,  
547 and olivine of our entire sample set. The contrasting information provided by petrographic and heavy-  
548 mineral analyses represents an apparently paradoxical case, which is produced whenever recycled  
549 detritus generated by a heavy-mineral poor sedimentary source mixes with minor quantities of first-  
550 cycle detritus supplied by a heavy-mineral rich source (figure 1 in [Garzanti and Andò, 2019](#)). In this  
551 case, local sedimentary sources as young as Quaternary ([Geyh and Thiedig, 2008](#)) also supply  
552 limestone grains, whereas the Plio-Quaternary Haruj al Aswad basaltic field ([Al-Hafdh and Elshaafi,](#)  
553 [2015](#)) contributes clinopyroxene and olivine but very few basaltic grains.

554 The sample collected west of the Air mountains (5610) is most distinct in all respects. It is the richest  
555 in feldspars and amphibole and yielded only two zircon grains in the entire 654-1569 Ma age range.  
556 Rather than additional first-cycle contribution from basement rocks such as the Assodé-Issalane  
557 amphibolite-facies metamorphic rocks or Renatt granite, the low P/F ratio and very low heavy-  
558 mineral concentration point at recycling of (i.e., derivation from) Paleozoic to Mesozoic sandstones  
559 exposed nearby (e.g., [Salze et al., 2018](#)).

560 Moroccan samples document additional contribution from local orogenic sources represented by the  
561 High Atlas and adjacent Anti-Atlas Mountains, including clinopyroxene from volcanic rocks and  
562 epidote, prehnite, and pumpellyite from very-low to low-grade metavolcanic rocks. Prehnite and  
563 pumpellyite are peculiar of this region, and do not occur in the similar tHM suite characterizing the  
564 northwestern El Djouf Erg of central Mauritania, which includes more ZTR minerals and less  
565 clinopyroxene.



566 The enrichment in garnet in dune sample 5616 collected in the middle of the Grand Erg Oriental is  
 1  
 567 puzzling (Table 1). This anomaly might be ascribed to local concentration of garnet by selective  
 3  
 568 removal of lower-density minerals, a process that may occur in this dune field characterized by  
 4  
 6  
 569 turbulent wind circulation. The widespread presence of star dunes in the erg (Telbisz and Keszler,  
 8  
 570 2018) lends support to this hypothesis.

11  
 571 Distinct composition also characterizes dunes along the Nile Valley, which include a few feldspars,  
 13  
 572 carbonate rock fragments and a few other sedimentary, metasedimentary and volcanic lithics, together  
 14  
 15  
 573 with a tHM suite ranging up to moderately poor and including epidote, amphibole, clinopyroxene,  
 16  
 18  
 574 staurolite, and minor garnet and kyanite. This indicates sediment mixing from various sources,  
 20  
 21  
 575 including the Saharan Metacraton, its Mesozoic to Cenozoic cover strata, and the Nile (Garzanti et  
 22  
 23  
 576 al., 2015a).

#### 26 577 578 6.6. Local sediment reworking

29  
 579 The considerations made above concern only sand derived from lithified source rocks. In desert  
 30  
 580 environments, however, the incessant wind action causes repeated and extensive reworking of  
 31  
 32  
 581 unconsolidated sediment, not only from the stoss side to the lee side of active dunes or from one  
 34  
 35  
 582 active dune to the next, but also from locally exhumed fossil dune fields. Major sources of wind-  
 36  
 37  
 583 reworked sediment are dry lake beds, found in diverse areas both within and at the periphery of the  
 38  
 39  
 584 desert and representing the record of a recent wetter past (Drake et al., 2011). Examples include the  
 40  
 41  
 585 active dunes dominated by gypsum grains found around Chott el Jerid at the northern edge of the  
 42  
 44  
 586 Sahara in Tunisia (Fig. 4B) and the abundant rounded mudclasts mixed with monocrystalline quartz  
 45  
 46  
 587 in dunes surrounding the Bodélé Depression in Chad (Fig.4F). Sediment deflated from lake beds,  
 47  
 48  
 588 however, dominantly consists of fine silt carried thousands of kilometers away as far as South  
 49  
 50  
 589 America and the Caribbean (Swap et al., 1992; Prospero, 1996).  
 51  
 52  
 590  
 56  
 57  
 591

### 58 59 592 7. Polycyclic nature of Saharan sands

593  
 60  
 61  
 62  
 63  
 64  
 65

### 594 7.1. Sand derived from sandstone

595

596 Saharan dune sand is almost invariably pure quartzose with very poor tHM suites dominated by  
 597 zircon, tourmaline, and rutile (Fig. 4, 5). Because these are the most mechanically and chemically  
 598 durable common minerals, and hence those most likely to survive more than a single sedimentary  
 599 cycle, quartz abundance and depleted tHM suites have long been used as indicators of the extent of  
 600 recycling (e.g., Hubert, 1962; Blatt, 1967). The monotonous mineralogical signature of dune sand all  
 601 across the Sahara thus points at provenance dominantly from siliciclastic rocks widely exposed  
 602 throughout the region and ranging in age from Paleozoic (Avigad et al., 2005; Meinhold et al., 2011;  
 603 Morton et al., 2011) to Mesozoic (e.g., “Nubian sandstone”; Selley, 1997; Carr, 2003), and Cenozoic  
 604 (Swezey, 2009).

605 Detrital-zircon geochronology studies of these sandstones (Table 2) documented the widespread  
 606 abundance of Neoproterozoic-aged zircon grains, indicating ultimate supply from the Pan-African  
 607 orogen including the Trans-Sahara belt. A subordinate Paleoproterozoic cluster was inferred to  
 608 indicate provenance from the West African Craton or perhaps Amazonia (Linnemann et al., 2011). A  
 609 Tonian age cluster characterizes feldspar-bearing Cambrian sandstones in Morocco (Avigad et al.,  
 610 2012). The common occurrence of ~1 Ga (“Grenvillian”) zircons in Paleozoic to Mesozoic  
 611 sandstones of southern Libya, lacking equivalents in igneous basements of northern Africa, has been  
 612 emphasized (Meinhold et al., 2011).

### 614 7.2. Comparing compiled datasets

615

616 Statistical tools are here applied to compare zircon-age data obtained on modern sands (Fig. 9) with  
 617 compiled age spectra from potential Paleozoic to Mesozoic parent sandstones exposed in northern  
 618 Africa (Fig. 10). The stack of KDE plots highlights the recurrence of the most prominent Ediacaran  
 619 (~0.6 Ga) peak in all compiled datasets (Fig. 10B). Among potential source rocks, most distinct is the  
 620 spectrum from Paleozoic-Mesozoic sandstones of southern Libya (Meinhold et al., 2011), which  
 621 display more prominent “Grenvillian” (~1 Ga), “Eburnean” (~2 Ga) and “Liberian” (Neoproterozoic)

622 peaks. More and slightly older Eburnean-aged zircons characterize Cambrian sandstones from  
 1  
 623 western Algeria (Wang et al., 2020). Most striking is the similarity of zircon-age spectra between  
 3  
 624 modern Saharan and Arabian dune sands. Besides the not many Mesozoic and Cenozoic zircons  
 4  
 6 occurring in dune fields close to Arabian Gulf shores and derived from the Anatolia Plateau and the  
 6  
 625 Zagros Mountains *via* the Euphrates-Tigris-Karun river system (Garzanti et al., 2016), differences  
 8  
 626 are limited to a few more ages around 0.8 Ga (a feature common to Nile sand; Fig. 9) and a few more  
 10  
 627 Neoproterozoic ages in Arabia.  
 11  
 628

16  
 629 The remarkable homogeneity of detrital-zircon age spectra all across Arabia and northern Africa is  
 18  
 630 confirmed by Multidimensional Scaling analysis. The central position of Saharan sands in MDS maps  
 20  
 631 (Fig. 10C,D) confirm that, as Arabian desert sands, they largely resulted from the homogenization of  
 22  
 632 detritus recycled from Paleozoic to Mesozoic parent sandstones. The MDS maps highlight that this  
 24  
 633 averaged zircon-age signal also characterizes Cambrian sandstones of southeastern Algeria, Morocco,  
 26  
 634 and central-western Libya (Linnemann et al., 2011; Avigad et al., 2012; Altumi et al., 2013), whereas  
 28  
 635 Paleozoic-Mesozoic sandstones of southern Libya (Meinhold et al., 2011) and Cambrian sandstones  
 30  
 636 from western Algeria (Wang et al., 2020) are distinct.  
 32  
 637

### 638 *7.3. Paleozoic sandstones as a major sand supplier for modern dunes*

639  
 40  
 640 Cambro-Ordovician and younger sandstones widely exposed across the Sahara represent a huge  
 42  
 641 reservoir of quartz grains to be recycled through time, finally ending up in modern dune fields. In  
 44  
 642 Saharan dune sand, zircon grains yielded mostly (77%) Neoproterozoic ages, consistently with  
 46  
 643 ultimate origin from the Pan-African orogen and the Trans-Saharan belt. Virtually the same zircon-age  
 48  
 644 spectra characterize dune sand across the Sahara, Nile River sand from Ethiopia and Sudan to Egypt,  
 50  
 645 and Arabian sand seas from the Great Nafud in the north to the giant Rub' al Khali in the south (Fig.  
 52  
 646 9).

54  
 647 Such a vast areal distribution of parent sandstones and daughter sands with similar mineralogical and  
 56  
 648 geochronological fingerprints reflects multiple recycling and homogenization at the wide spatial scale  
 58  
 60  
 61  
 62  
 63  
 64  
 65

649 of the whole northern Africa and Middle East throughout the Phanerozoic. After the major Pan-  
 1 African mountain-building event and the tectonic activity that followed (e.g., [Stern, 1985](#)), the large  
 650 volume of newly produced crustal material was extensively eroded and repeatedly recycled until the  
 4  
 651 present day.  
 6  
 652

8  
 9  
 653 Besides the dominant Neoproterozoic double peak, [Meinhold et al. \(2013\)](#) noted that Grenvillian-  
 10 aged zircons become more common from Morocco and Algeria to Libya, and from Cambrian to  
 11  
 654 Middle Ordovician strata in Libya. Such an eastward trend is reflected in zircon-age spectra of dune  
 14  
 655 sand, showing a southeastward increase in the relative abundance of Stenian-age zircons from Mali,  
 16  
 656 Mauritania, western Niger and Morocco ( $\leq 5\%$  of total ages) to central-eastern Niger, Chad, Libya,  
 18  
 657 and Egypt (3-16% of total ages; [Fig. 7](#)).  
 19  
 658

## 659 **8. Relationships between sand mineralogy and sedimentary processes in desert environments**

660  
 27  
 661 The origin of sand in large dune fields represents a still poorly understood controversial issue. In  
 29  
 662 many Earth's deserts, aeolian sand is enriched in most durable quartz and ZTR minerals ([Muhs,](#)  
 31  
 663 [2004](#)), but such a simple monotonous compositional signature hardly facilitates interpretation,  
 34  
 664 because it is the resultant of the combined effects of diverse processes accumulated through  
 36  
 665 geological time ([Dott, 2003](#)). Prominence of physical factors or of chemical processes? Selective  
 38  
 666 break-down of less durable grains by mechanical abrasion, pre-depositional weathering, or intrastratal  
 39  
 667 dissolution? This is the crux of the "quartzarenite problem" ([Basu, 2020](#)).  
 41  
 668

45  
 46  
 669 In this section, we review the relationships between sand mineralogy and sedimentary processes in  
 48  
 670 desert environments, placing emphasis on *in situ* sand generation by wind erosion *versus* external  
 50  
 671 fluvial supply. In the former case, most sand results from disaggregation of rocks with high sand-  
 51  
 672 generation potential, such as sandstones or locally granites, and will thus be primarily composed of  
 53  
 673 quartz and locally feldspars with generally very poor heavy-mineral suites largely consisting of ZTR  
 56  
 674 minerals. In the latter case, mineralogy is variable, with larger percentages of first-cycle detritus  
 57  
 60  
 61  
 62  
 63  
 64  
 65



675 derived from a wide range of source rocks, including lithic fragments as well as amphibole, epidote,  
 1  
 676 garnet, or pyroxene.  
 3

4  
 677

### 678 ***8.1. Wind-fed quartz-rich sand seas***

7  
 679

680 Sand seas consisting of pure quartzose sand are well documented in the Paleozoic (e.g., [Dott et al.,](#)  
 10  
 681 [1986](#)), Mesozoic (e.g., [Bertolini et al., 2020](#)), and Cenozoic (e.g., [Vainer et al., 2018](#)). Although the  
 12  
 682 Sahara has several predecessors in geological history, characterized by the same monotonous  
 13  
 683 compositional signature dominated by the most durable minerals, the Sahara cannot be considered  
 17  
 684 the rule in this respect, but rather an end-member case.  
 19

20

685 The debate on the existence of first-cycle quartzarenites went on for long ([Krynine, 1941](#); [Suttner et](#)  
 22  
 686 [al., 1981](#); [Johnsson, 1993](#)), until the modern-sand lesson indicated unambiguously that sand  
 23  
 687 consisting virtually entirely of quartz and ZTR minerals cannot be the result of mechanical or  
 27  
 688 weathering processes even in the most aggressive climatic conditions met in modern Earth, but that  
 28  
 689 the final cleansing of less stable minerals requires extensive intrastratal dissolution, i.e., inheritance  
 30  
 690 from previous sedimentary cycles of weathering and diagenesis ([Garzanti et al., 2019a](#)). Pure  
 34  
 691 quartzose composition thus implies that sand originated from homogenization of detritus chiefly  
 35  
 692 produced by physical disaggregation of quartz-rich parent sandstones, possibly derived in turn from  
 37  
 693 older granparent sandstones, along a line of ancestry rooted in the deep past.  
 40  
 41

42

694 The Sahara is an example of a vast desert hosting sand purified during multiple steps through  
 44  
 695 Phanerozoic time. No clear trace is left of sediment supplied by rivers draining towards the desert,  
 45  
 696 with the exception of Moroccan dunes at the foot of the Anti-Atlas Mountains and of pyroxene-  
 47  
 697 enriched Egyptian dunes near Aswan and east of the Nile ([Garzanti et al., 2015a](#) p.45). Conversely,  
 51  
 698 aeolian sand is overwhelming. Rather than the river supplying sand to the desert, it is the dune field  
 52  
 699 that commonly invades and chokes the dry river valley, as seen in northeastern Egypt and Sinai  
 54  
 700 ([Garzanti et al., 2015a](#) p.46). In hyperarid climate, river action may be weakened to the point that  
 56  
 701 fluvial contribution to the dune field becomes insignificant, as documented in northern Arabia, where  
 58  
 59  
 60  
 61  
 62  
 63  
 64  
 65

702 sand is dominantly supplied by disaggregation of Cambro-Ordovician quartzarenites and no river  
 1  
 703 influences the mineralogy of dune sand if not minimally (< 5%) and near the site where it empties  
 3  
 704 into the desert (Garzanti et al., 2013 p.13).  
 4  
 5  
 6

## 705 706 **8.2. River-fed lithic-bearing sand seas**

707  
 708 The opposite end-member is represented by sand seas supplied by a major river, as indicated by sand  
 12  
 709 mineralogy maintaining the same characteristic fingerprints of the fluvial feeding system through  
 13  
 15  
 710 distances up to a thousand of kilometers. These deserts can be considered as wind-reworked inland  
 17  
 18  
 711 or coastal deltas. An emblematic case is represented by the coastal ergs of southwestern Africa, which  
 19  
 20  
 712 are mostly fed *via* northward littoral drift from the Orange River mouth. Dune sand of the coastal  
 22  
 713 Namib Erg (southern Namibia) is estimated to be 99% derived from the Orange River even at its  
 23  
 24  
 25  
 714 farthest northern edge, the main mineralogical and textural differences being a slightly enrichment in  
 27  
 715 quartz at the expense of most easily destroyed sedimentary and metasedimentary lithics, a dearth of  
 28  
 29  
 30  
 716 mica, and a markedly higher degree of grain roundness (Garzanti et al., 2012, 2015b). Because of  
 32  
 717 hyperarid climate, additional fluvial supply is limited along the coast. Consequently, coastal ergs in  
 34  
 718 northern Namibia to southern Angola are still dominantly derived (~80% and ~60%, respectively)  
 35  
 36  
 37  
 719 from the Orange River mouth after a multistep longshore transport up to 1800 km (Garzanti et al.,  
 39  
 720 2014a, 2018c). All along, composition of dune sand remains constantly feldspatho-quartzose with  
 40  
 41  
 42  
 721 common basaltic rock fragments and rich tHM suites containing high, although progressively diluted,  
 44  
 722 percentages of clinopyroxene.  
 45  
 46

47  
 723 Fluvial-dominated dune fields tend to be the rule in orogenic settings. Several examples are  
 49  
 724 documented in arid inland areas across Asia, where river sediments are trapped in subsiding troughs  
 51  
 725 adjacent to the front of active orogens such as the Kopeh-Dagh, Kun Lun, Altyn Tagh, Tian Shan, or  
 52  
 53  
 54  
 726 the western Himalaya. The Karakum Desert in Turkmenistan contains feldspatho-litho-quartzose  
 56  
 727 dune sand with varied lithic population and moderately rich epidote-amphibole-garnet tHM suite,  
 57  
 58  
 59  
 60  
 61  
 62  
 63  
 64  
 65

728 which closely matches sand of the Amu Darja River draining the western Pamir mountains of  
 1 Tajikistan ([Garzanti et al., 2019b](#)).

730 Dune sand of the Thal Desert in central Pakistan contains subequal amounts of quartz, feldspars, and  
 6 mostly metamorphic and sedimentary lithic fragments, as well as a very rich amphibole-epidote-  
 731 garnet-pyroxene tHM suite ([Liang et al., 2019](#)). This low-quartz signature indicates supply from the  
 9 upper Indus River at latest Pleistocene/early Holocene times, when erosion was focused on the high  
 10 mountains of northern Pakistan ([Garzanti et al., 2020](#)).

16 The large Taklamakan Desert of northwestern China contains feldspatho-litho-quartzose sand with  
 1735 mainly sedimentary and metamorphic lithics and moderately rich amphibole-epidote-pyroxene tHM  
 18 suite, a composition virtually indistinguishable from sand of the Yarkhand River draining the northern  
 1936 Karakorum and Kun Lun Mountains ([Rittner et al., 2016](#)).

### 26 **8.3. Fluvial/aeolian connectivity in arid environments**

2739 The interaction between fluvial supply and wind reworking is documented at the periphery of all sand  
 2840 seas. Excellent examples are represented by the eastward landward side of Namibian deserts, where  
 29 the conflict between persistent wind action and episodic river floods produces spectacular sedimentary  
 30 features ([Stanistreet and Stollhofen, 2002](#); [Svendsen et al., 2003](#); [Feder et al., 2018](#)). In the Kalahari  
 31 Desert, Sahara's brother in southern hemisphere Africa, dune sand is also largely pure quartzose but  
 32 composition is not equally homogeneous, and distinct mineralogy in different areas reflects a greater  
 33 role of fluvial supply ([Garzanti et al., 2014b](#)). Kalahari dune fields are best developed west of river  
 34 channels, suggesting deflation of fluvial sediments by easterly winds during drier periods ([Shaw and](#)  
 35 [Goudie 2002](#)). Conversely, rivers have inundated interdune areas and incised their course across dune  
 36 ridges during wetter periods ([Thomas et al. 2000](#)). Quartz grains are commonly well rounded in both  
 37 dune and river sands, documenting aeolian abrasion at one or more stages of their multistep transport  
 38 history. Climate-controlled cycling of quartzose sand from the fluvial to the aeolian environment and  
 39 back has taken place repeatedly in the Kalahari ([Thomas and Shaw 2002](#)).

755 In Saudi Arabia, dune sand remains homogeneously quartz-rich feldspatho-quartzose to quartzose  
 1  
 756 across the Rub'Al Khali, the largest continuous sand sea on Earth, but compositional variations are  
 3  
 757 observed along the desert's rims. Dune sand becomes lithic carbonaticlastic close to the Hadhramaut  
 4  
 6  
 758 carbonate tableland in Yemen to the south and quartzo-lithic carbonaticlastic along the Gulf shores  
 8  
 759 of the Emirate of Abu Dhabi to the northeast (Garzanti et al., 2001, 2003). Fluvial interactions are  
 10  
 11  
 760 documented at the southwestern edge of the sand sea, where dune sand is less quartz-rich than in  
 13  
 14  
 761 Cambro-Ordovician parent sandstones, has distinctly higher heavy-mineral concentration, higher  
 15  
 16  
 762 amphibole, and lower ZTR indices, indicating that *wadi*-derived first-cycle detritus from the  
 18  
 19  
 763 crystalline basement accounts for ~20% of aeolian sand (Garzanti et al., 2017).  
 20  
 21  
 764 Fluvial-aeolian connectivity is well documented in the Thar Desert of southern Pakistan, where sand  
 23  
 24  
 765 was exchanged over spatial scales of hundreds of kilometers between the Indus River and the desert.  
 25  
 26  
 766 Summer monsoon winds recycle sediment from the lower Indus River and delta downwind and  
 27  
 28  
 767 upstream. Large volumes of sediment were thus stored inland since the mid-Holocene, when the  
 30  
 31  
 768 desert expanded as the summer monsoon rainfall decreased, buffering the sediment flux to the ocean  
 32  
 33  
 769 (East et al., 2015).  
 35  
 36  
 770 Another renowned example of fluvial-aeolian interaction is provided by the sand seas and loess  
 37  
 38  
 771 plateau of northern China, where the accumulated sand and dust have been largely transported  
 40  
 41  
 772 originally by the Yellow River from the northern Tibetan Plateau (Stevens et al., 2013; Nie et al.,  
 42  
 43  
 773 2015). Contrariwise, aeolian sediment is widely supplied to the Yellow River in Inner Mongolia,  
 44  
 45  
 774 where the river course is largely incised within loess deposits and flanked by a wide desert area from  
 47  
 48  
 775 where aeolian sand is blown periodically toward the fluvial channel by the winter monsoon (Pang et  
 49  
 50  
 776 al., 2018). Such a multistep, back-and-forth sediment mixing contributes to extensive homogenization  
 52  
 53  
 777 of compositional fingerprints of fluvial sand, dune sand, and loess deposits.  
 54  
 55

#### 5779 **8.4. Aeolian processes able to modify sand mineralogy and texture** 58 59 60 61 62 63 64 65



781 Distinguishing end-member types of deserts may appear as a largely conceptual exercise, because  
1  
782 landscapes evolve through time under the complex effects of climate change, which controls wind  
3  
783 strength, fluvial runoff, water-table level, and vegetation cover. Despite Nature's complexities,  
4  
6  
784 however, a basic distinction holds between river-fed sand seas with varied mineralogy including first-  
8  
785 cycle detritus (most typical of orogenic settings) *versus* sand seas fed *in situ* by recycling of older  
10  
786 sandstones and characterized by distilled composition dominated by quartz and ZTR minerals (most  
11  
13  
787 typical of anorogenic settings).  
14  
15  
16  
788 Because arid climate hampers the effectiveness of chemical reactions, processes that can alter  
18  
789 sediment composition within a desert are essentially physical, including abrasion and wind sorting.  
20  
21  
790 Recycling *per se* can only replicate the mineralogy of parent clastic units in the daughter sand, but by  
22  
23  
791 this fundamentally physical mechanism the effects of selective chemical and mechanical breakdown  
25  
26  
792 of labile grains can be accumulated through multiple sedimentary cycles, and inherited in the next  
27  
28  
793 ([Garzanti, 2017](#)).  
30  
31  
794 As a most evident effect of mechanical abrasion and comminution, softer detrital grains effectively  
32  
33  
795 increase their roundness in aeolian dunes as a consequence of repeated impacts with harder grains in  
35  
796 air ([Resentini et al., 2018](#)). Clear examples are seen in the Rub'al Khali, where carbonate grains are  
37  
38  
797 most readily rounded with transport distance, progressively reduced in size, and finally removed.  
40  
41  
798 Other minerals, cleaved or softer than quartz or garnet like feldspars, rock fragments or  
42  
43  
799 ferromagnesian silicates, may also be selectively comminuted and concentrated in finer size fractions  
44  
45  
800 ([Garzanti et al., 2017](#)).  
47  
48  
801 Selective entrainment and winnowing are other physical processes that can markedly affect sand  
49  
50  
802 mineralogy. Deflation by strong winds selectively removes slow-settling detrital components, leaving  
52  
53  
803 behind coarser layers (e.g., granule ripples) or laminae enriched in ultradense minerals such as garnet  
54  
55  
804 and magnetite. Contrary to mechanical abrasion and comminution, these modifications are largely  
56  
57  
805 temporary and reversible.  
59  
60  
806

## 807 9. Conclusions

808

809 The Sahara is a vast desert. Its composite structure includes large dune fields hosted in sedimentary  
810 basins separated by elevated areas exposing the roots of Precambrian orogens or created by recent  
811 intraplate volcanism. Such an heterogeneity of landscapes and geological formations is contrasted by  
812 a remarkably homogeneous composition of dune sand, consisting almost everywhere of > 95% quartz  
813 and durable minerals such as zircon, tourmaline, and rutile. Exceptions are recorded only locally in  
814 the vicinity of volcanic fields (e.g., Haruj al Aswad in Libya), basement highs (e.g., Aïr Mountains  
815 in Niger), fold belts (Anti-Atlas in Morocco), or along the Nile Valley. Everywhere else, from Lake  
816 Chad and the Bodélé Depression to the great ergs of Algeria, and from the Western Desert of Egypt  
817 to the Atlantic coast of Mauritania, dune sand has almost the same, monotonous, pure quartzose  
818 composition. Besides U-Pb age spectra of detrital zircons, which reveal a significant difference  
819 between the southeastern part of the desert characterized by a more pronounced ~1 Ga peak *versus*  
820 the northwestern part where Paleoproterozoic ages are more common and some Paleozoic and  
821 Mesozoic ages occur, our data do not show any compositional trend that could be compared with the  
822 main directions of present or past atmospheric circulation and wind transport.

823 The composition and homogeneity of Saharan dune sand reflect similar generative processes and  
824 source rocks, and extensive recycling repeated through geological time after the end of the  
825 Neoproterozoic, which zircon-age spectra indicate as the last major event of crustal growth in the  
826 region. Subsequently, the newly formed Arabian-Nubian Shield was covered by quartz-rich  
827 siliciclastic sediments extending all across the area from Oman to Mauritania and beyond. It is from  
828 this thick blanket of sandstone that large volumes of quartzose sand were generated, and enriched  
829 progressively in durable minerals during the multiple cycles of erosion, sedimentation and diagenesis  
830 that took place in the long period of relative tectonic quiescence that characterized the entire  
831 Phanerozoic in this region. The geographic zircon-age distribution in daughter sands thus chiefly  
832 reflects the zircon-age distribution in parent sandstones (i.e., different patterns between southeast and

northwest), and hence sediment dispersal systems existing at those times rather than present wind patterns (i.e., separation of sand flow between north and south).

Because zircon is durable, the larger part of zircon grains contained in most sediment samples is likely to be recycled from sedimentary covers rather than derived first-cycle from basement rocks. In provenance studies based on detrital-zircon ages, the assumption that observed age patterns reflect transport pathways existing at the time of deposition rather than inheritance from even multiple and remote landscapes of the past thus needs to be carefully investigated and convincingly demonstrated rather than implicitly assumed.

## ACKNOWLEDGMENTS

We warmly thank Charlie Bristow, Luca Baglioni, Raffaele Bitonte, Stefano Del Fraro, Riccardo Graziadei, Laura Fielding, Yani Najman, Ada Ali Abdel Megid, and Diego Roncoroni for providing samples from various Saharan dune fields. Editor Chris Fielding and reviewers Abhijit Basu, Tim Lawton, Luca Caracciolo, and Anonymous#4 provided very careful constructive critical advice. This study was supported by MIUR – Dipartimenti di Eccellenza 2018–2022, Department of Earth and Environmental Sciences, University of Milano-Bicocca. TB is supported by the Natural Environment Research Council through grant NE/L002485/1.

## SUPPLEMENTARY MATERIALS

Supplementary data associated with this article, to be found in the online version at [http://dx.doi.\\_\\_\\_\\_\\_](http://dx.doi._____), include information on sampling sites (Table A1) together with sand-petrography (Table A2) and heavy-mineral data (Table A3). The complete detrital-zircon geochronology dataset is presented in Appendix B. Additional statistical tools are illustrated in Appendix C. The Google-Earth™ map of sampling sites Sahara.kmz is also provided.

860 **FIGURE AND TABLE CAPTIONS**

1  
2  
861 **Figure 1.** The Sahara Desert in northern Africa. Main dune fields, sedimentary basins, and geological  
4  
862 domains are indicated. Sampling sites are shown with circles coloured by region. CeJ = Chott el Jerid  
6  
863 (Tunisia); HaA = Haruj al Aswad (Libya).

9  
10  
864 **Figure 2.** Sand flow patterns obtained by interpolation of meteorological and bedform data (grain-  
12  
865 size range 50-100  $\mu\text{m}$ ; modified after [Wilson, 1971](#)). The calculated divide (dashed red line) nearly  
14  
866 corresponds to the southern boundary of the subtropical high-pressure zone; peaks P1 (Tademait), P2  
17  
867 (Hoggar), and P3 (Libyan) correspond to high-pressure centres from which sand flow radiates, and  
20  
868 saddles S1 (Erg Chech), S2 (Tanezrouf), and S3 (Teneré) correspond to possible sand flow corridors.  
22  
869 Mountain areas in brown, with indicated highest elevation for each; sample locations coloured as in  
24  
870 [Fig. 1](#).

27  
28  
871 **Figure 3.** Geology of the Sahara (modified after [CGMW-BRGM, 2016](#)). Major tectonic domains are  
30  
872 separated by dashed lines. Sample locations coloured as in [Fig. 1](#). ANS = Arabian-Nubian Shield.

33  
34  
873 **Figure 4.** Compositional variability of Saharan dune sand (photos arranged in geographical order  
36  
874 from NW to SE). **A)** Common sedimentary/low-rank metasedimentary lithics (*Ls*, *Lms*) with minor  
39  
875 microlitic volcanic rock fragments (*Lv*) and perthitic K-feldspar (*K*) derived from nearby orogenic  
41  
876 sources. **B)** Gypsum clasts (*g*) reworked from the adjacent salt lake. **C)** Common limestone grains (*e*  
44  
877 = echinoid spine) with clinopyroxene (*p*) and olivine (*o*) derived from the Haruj al Aswad basaltic  
46  
878 field. **D)** Common polycrystalline quartz (*Qp*) associated with up to well-rounded or etched  
48  
879 monocrystalline quartz. **E)** Up to well-rounded or etched quartz associated with plagioclase (*P*) and  
51  
880 K-feldspar (*K*). **F)** Up to well-rounded quartz with abundant mudclasts (*m*) reworked from the dry  
53  
881 bed of once Mega-Lake Chad. **G)** Dominant, up to well-rounded monocrystalline quartz. **H).**  
56  
882 Common K-feldspar (*M* = cross-hatched microcline) and plagioclase (*P*); quartz with abraded  
58  
59  
60  
61  
62  
63  
64  
65



883 overgrowths (*arrow*) indicates recycled origin. **I**) Dominant, up to well-rounded monocrystalline  
 1 quartz. All photos with crossed polars; blue bar for scale = 100  $\mu\text{m}$ .

885 **Figure 5.** Petrography of Sahara dune sand. Most samples are monotonously pure quartzose (*pQ*;  
 7 plotting in blue fields of QFL and QPK diagrams), with K-feldspar prevailing over plagioclase and  
 886 negligible lithics. A few samples are quartzose, (*Q*) quartz-rich feldspatho-quartzose (*qFQ*), or  
 10 quartz-rich litho-quartzose sedimentaelastic (*qLQ*; W of Nile Valley, S of Anti-Atlas in Morocco, NE  
 888 Murzuq Erg in Libya). Q = quartz; F = feldspars (P = plagioclase; Or\* = untwinned K-feldspar; Mic\*  
 15 = cross-hatched microcline); L = lithic fragments (Lm = metamorphic; Lv = volcanic; Ls =  
 889 sedimentary).

892 **Figure 6.** Heavy minerals in Saharan dune sand. The biplot highlights that tHM suites are mixtures  
 25 of three main mineral groups: 1) largely recycled durable ZTR; 2) the orogenic triad amphibole,  
 893 epidote and garnet; 3) volcanic-derived clinopyroxene and olivine. ZTR minerals are dominant in the  
 27 southern Sahara, with amphibole and locally staurolite increasing close to the Aïr Mountains in Niger  
 894 (5610). In the northern Sahara, clinopyroxene occurs more frequently and a clinopyroxene-olivine  
 30 suite characterizes dunes near the Haruj al Aswad volcanic field in Libya (NE Murzuq Erg, 5584).

898 **Figure 7.** U-Pb age spectra of detrital zircons (age vs. frequencies plotted as Kernel Density Estimates  
 41 using the *provenance* package of Vermeesch et al., 2016). All samples display the characteristic  
 899 Neoproterozoic “double-peak”, with minor Paleoproterozoic and Archean ages. Paleozoic and  
 43 Mesozoic clusters occur west of the Air Mountains and in Burkina Faso, respectively. Cenozoic ages  
 900 are found in Algeria and Mauritania and are locally as young as 5-6 Ma in Morocco and Niger.

903 **Figure 8.** Multivariate statistical analysis (detailed explanation in subsection 4.4). **A**) CA for  
 54 petrographic (PT) dataset. **B**) CA for heavy-mineral (HM) dataset. **C**) MDS for detrital-zircon (DZ)  
 904 ages. **D**) INDSCAL for combined PT and HM datasets. Group configuration is expressed by  
 57 perpendicular arrows and depict the direction of variability for each dataset. **E**) Hierarchical  
 905

907 clustering dendrogram (height refers to normalised distance units produced by GPA of PT, HM, and  
 1  
 908 DZ datasets; [Garzanti and Vermeesch, 2015](#)). **F**) Generalised Procrustes Analysis (GPA) of PT, HM  
 3  
 909 and DZ datasets (symbol shapes refer to cluster analysis in **E** and colours to geographical location).  
 4  
 5  
 6  
 910 For **A**, **B**, and **C**, sample locations are shown on the sand flow map below; clusters refer to hierarchical  
 8  
 911 clustering ([Appendix C](#)); axes units are normalised values based on chi-square distance for **A** and **B**,  
 10  
 912 and on Kolmogorov-Smirnov distance for **C**.  
 11  
 12  
 13  
 14

913 **Figure 9.** U-Pb zircon-age spectra are not only remarkably monotonous all across the Sahara, but do  
 15  
 914 not differ significantly from either Nile sand in Sudan to Egypt or from Arabian desert sands (data  
 17  
 18  
 19  
 915 after [Garzanti et al., 2013, 2017, 2018b](#); age vs. frequencies plotted as Kernel Density Estimates using  
 21  
 916 the *provenance* package of [Vermeesch et al., 2016](#)). Zircon grains are massively recycled from post-  
 22  
 23  
 24  
 917 Pan-African siliciclastic units all across from the Arabian Gulf to the Atlantic Ocean. AHD = Aswan  
 26  
 918 High Dam, closed in 1964.  
 27  
 28  
 29  
 30

919 **Figure 10.** Statistical analysis based on compiled detrital-zircon ages presented in [Table 2](#). **A**) Sample  
 31  
 920 locations and sand flow map. **B**) Cumulative KDE plot of all concordant ages from this study (neon  
 33  
 34  
 35  
 921 red) compared with KDE plots of compiled datasets (peak height normalized to maximum peak of  
 37  
 922 each dataset; bandwidth maintained constant for all datasets). **C**, **D**) MDS maps comparing the  
 38  
 39  
 40  
 923 compiled zircon-age datasets with the cumulative age spectrum from this study (**C**), and with age  
 42  
 924 spectra for each sample group presented in [Fig. 7 \(D\)](#). Axes units are normalised values based on  
 44  
 925 Kolmogorov-Smirnov distance, with 90% confidence polygons represented by dashed red lines. Solid  
 46  
 926 and dashed black lines link closest and second-closest neighbours, respectively. Shepard's plot shown  
 48  
 927 in lower left corner.  
 50  
 51  
 52  
 53

928 **Table 1.** Petrography and heavy minerals in Saharan dune sands. Q = quartz; F = feldspars (P =  
 54  
 929 plagioclase); L = lithic grains (Lv = volcanic; Lc = carbonate; Lsm = other sedimentary and  
 56  
 57  
 58  
 930 metasedimentary). Transparent heavy minerals (tHMC) include: ZTR = zircon + tourmaline + rutile;  
 60  
 931 Ap = apatite; Ttn = titanite; Ep = epidote; P&P = prehnite + pumpellyite; Grt = garnet; St = staurolite;  
 62  
 63  
 64  
 65

932 Ky = kyanite; Amp = amphibole; Px = pyroxene; Ol = olivine; &tHM = others (anatase, sillimanite,  
1  
933 andalusite, monazite, topaz, brookite). Full information on counted grains is provided in [Appendix](#)  
3  
4  
934 [Tables A2](#) and [A3](#).

935 **Table 2.** Compilation of ages of detrital zircons contained in Phanerozoic sedimentary rocks and  
9  
10  
936 modern dunes from northern Africa and Arabia. Age range is in Ga and percentage of grain ages are  
11  
12  
937 provided for each cluster.

14  
15  
16  
17  
18  
19  
20  
21  
22  
23  
24  
25  
26  
27  
28  
29  
30  
31  
32  
33  
34  
35  
36  
37  
38  
39  
40  
41  
42  
43  
44  
45  
46  
47  
48  
49  
50  
51  
52  
53  
54  
55  
56  
57  
58  
59  
60  
61  
62  
63  
64  
65

938 **REFERENCES**

- 939  
940 Abdelhak, M., Ahmed, K., Abdelkader, B., Brahim, Z., Rachid, K., 2014. Algerian Sahara sand dunes  
941 characterization. *Silicon* 6, 149-154.
- 942 Abdelkareem, M., El-Baz, F., 2015. Regional view of a trans-African drainage system. *Journal of*  
943 *Advanced Research* 6, 433-439.
- 944 Abdelsalam, M.G., 2018. The Nile's journey through space and time: A geological perspective. *Earth-*  
945 *Science Reviews* 177, 742-773.
- 946 Abdelsalam, M.G., Liégeois, J.P., Stern, R.J., 2002. The Saharan Metacraton. *Journal of African*  
947 *Earth Sciences* 34, 119-136.
- 948 Abouchami, W., Boher, M., Michard, A., Albarede, F., 1990. A major 2.1 Ga event of mafic  
949 magmatism in West Africa: an early stage of crustal accretion. *Journal of Geophysical Research:*  
950 *Solid Earth* 95, 17605-17629.
- 951 Al-Gamal, S.A., 2011. An assessment of recharge possibility to North-Western Sahara Aquifer  
952 System (NWSAS) using environmental isotopes. *Journal of Hydrology*, 398, 184-190.
- 953 Al-Hafdh, N.M., Elshaafi, A.E.S.S., 2015. Geochemistry and petrology of basic volcanic rocks of  
954 Jabal Al Haruj Al-Aswad, Libya. *International Journal of Geosciences* 6, 109-144.
- 955 Altumi, M.M., Elicki, O., Linnemann, U., Hofmann, M., Sagawe, A., Gärtner, A., 2013. U–Pb LA-  
956 ICP-MS detrital zircon ages from the Cambrian of Al Qarqaf Arch, central-western Libya:  
957 Provenance of the West Gondwanan sand sea at the dawn of the early Palaeozoic. *Journal of*  
958 *African Earth Sciences* 79, 74-97.
- 959 Andò, S., 2020. Gravimetric separation of heavy-minerals in sediments. *Minerals* 10(3), 273,  
960 doi:10.3390/min10030273.
- 961 Arbuszewski, J.A., deMenocal, P. B., Cléroux, C., Bradtmiller, L., Mix, A., 2013. Meridional shifts  
962 of the Atlantic intertropical convergence zone since the Last Glacial Maximum. *Nature*  
963 *Geoscience* 6, 959-962.
- 964 Avigad, D., Sandler, A., Kolodner, K., Stern, R. J., McWilliams, M., Miller, N., Beyth, M., 2005.  
965 Mass-production of Cambro–Ordovician quartz-rich sandstone as a consequence of chemical  
966 weathering of Pan-African terranes: environmental implications. *Earth and Planetary Science*  
967 *Letters* 240, 818-826.
- 968 Avigad, D., Gerdes, A., Morag, N., Bechstädt, T., 2012. Coupled U–Pb–Hf of detrital zircons of  
969 Cambrian sandstones from Morocco and Sardinia: implications for provenance and Precambrian  
970 crustal evolution of North Africa. *Gondwana Research* 21, 690-703.
- 971 Bagnold, R.A., 1942. *The physics of blown sand and desert dunes*. Methuen & Co., Ltd., London,  
972 265 p.
- 973 Baird, T., Bristow, C. S., Vermeesch, P., 2019. Measuring Sand Dune Migration Rates with COSI-  
974 Corr and Landsat: Opportunities and Challenges. *Remote Sensing* 11, 2423.

- 975 Bakker, N.L., Drake, N.A., Bristow, C.S., 2019. Evaluating the relative importance of northern  
976 African mineral dust sources using remote sensing. *Atmospheric Chemistry and Physics* 19(16),  
977 10525–10535.
- 978 Basu, A., 2020. Chemical weathering, first cycle quartz sand, and its bearing on quartz arenite.  
979 *Journal Indian Association of Sedimentologists* 37(2), 3-14.
- 980 Bertolini, G., Marques, J.C., Hartley, A.J., Da- Rosa, A.A., Scherer, C.M., Basei, M.A., Frantz, J.C.,  
981 2020, Controls on Early Cretaceous desert sediment provenance in south- west Gondwana,  
982 Botucatu Formation (Brazil and Uruguay). *Sedimentology* 67(5), 2672-2690.
- 983 Bertrand, J.M.L., Caby, R., 1978. Geodynamic evolution of the Pan-African orogenic belt: a new  
984 interpretation of the Hoggar shield (Algerian Sahara). *Geologische Rundschau* 67, 357-388.
- 985 Bird, P., 1979. Continental delamination and the Colorado Plateau. *Journal of Geophysical Research*  
986 84, 7561-7571.
- 987 Birkett, C. M., 2000. Synergistic remote sensing of Lake Chad: Variability of basin inundation.  
988 *Remote sensing of Environment* 72, 218-236.
- 989 Black, R., 1965. Sur la signification pétrogénétique de la découverte d'anorthosites associées aux  
990 complexes subvolcaniques du Niger. *Comptes rendus de l'Académie des Sciences* 260, 5829-  
991 5832.
- 992 Black, R., Caby, R., Moussine-Pouchkine, A., Bayer, R., Bertrand, J.M., Boullier, A.M., Fabre, J.,  
993 Lesquer, A., 1979. Evidence for late Precambrian plate tectonics in West Africa. *Nature* 278,  
994 223-227.
- 995 Blatt, H., 1967. Provenance determinations and recycling of sediments. *Journal of Sedimentary*  
996 *Petrology* 37, 1031-1044.
- 997 Boullier, A.M., Rocci, G., Cosso, N.Y., 1991. La chaîne pan-africaine d'Aouzegeur en Aïr (Niger):  
998 un trait majeur du bouclier Touareg. *Comptes rendus Académie des Sciences de Paris* 313, 63-  
999 68.
- 1000 Breed, C.S., Fryberger, S.G., Andrews, S., McCauley, C., Lennartz, F., Gebel, D., Horstman, K.,  
1001 1979. Regional studies of sand seas using Landsat (ERTS) imagery. A study of global sand seas.  
1002 US Geological Survey, Professional Paper 1052, 305-397.
- 1003 Brenchley, P.J., Marshall, J.D., Carden, G.A.F., Robertson, D.B.R., Long, D.G.F., Meidla, T., Hints,  
1004 L., Anderson, T.F., 1994. Bathymetric and isotopic evidence for a short-lived Late Ordovician  
1005 glaciation in a greenhouse period. *Geology* 22, 295-298.
- 1006 Bristow, C.S., Armitage, S.J., 2016. Dune ages in the sand deserts of the southern Sahara and Sahel.  
1007 *Quaternary International* 410, 46-57.
- 1008 Bristow, C.S., Drake, N., Armitage, S., 2009. Deflation in the dustiest place on Earth: the Bodélé  
1009 Depression, Chad. *Geomorphology* 105, 50-58.
- 1010 Bumby, A.J., Guiraud, R., 2005. The geodynamic setting of the Phanerozoic basins of Africa. *Journal*  
1011 *of African Earth Sciences* 43, 1-12.



- 1012 Burke, K., 1999. Tectonic significance of the accumulation of the voluminous early Paleozoic  
1013 reservoir containing quartz-rich sandstones of North Africa and Arabia. *Bulletin of the*  
1014 *Geological Society Houston*, 11-13.
- 1015 Caby, R., Andreopoulos-Renaud, U., Pin, C., 1989. Late Proterozoic arc–continent and continent–  
1016 continent collision in the Pan-African Trans-Saharan Belt of Mali. *Canadian Journal of Earth*  
1017 *Sciences* 26, 1136-1146.
- 1018 Caby, R., Bertrand, J.M.L., Black, R., 1981. Pan-African ocean closure and continental collision in  
1019 the Hoggar-Iforas segment, central Sahara. *Precambrian Plate Tectonics* 16, 407-434.
- 1020 Capot-Rey, R., 1945. Dry and humid morphology in the Western Erg. *Geographical Review* 35, 391-  
1021 407.
- 1022 Carr, I.D., 2003. A sequence stratigraphic synthesis of the North African Mesozoic. *Journal of*  
1023 *Petroleum Geology* 26, 133-152.
- 1024 Carroll, J.D., Chang, J.J., 1970. Analysis of individual differences in multidimensional scaling via an  
1025 N-way generalization of Eckart–Young decomposition. *Psychometrika* 35, 283–319.
- 1026 CGMW-BRGM, 2016. Geological Map of Africa, 1:10 million scale. Thiéblemont, D. et al. (eds.),  
1027 [www.brgm.fr](http://www.brgm.fr).
- 1028 Chikhaoui, M., Dupuy, C., Dostal, J., 1978. Geochemistry of late Proterozoic volcanic rocks from  
1029 Tassendjanet area (N.W. Hoggar, Algeria). *Contributions to Mineralogy and Petrology* 66, 157-  
1030 164.
- 1031 Coe, M.T., Foley, J.A., 2001. Human and natural impacts on the water resources of the Lake Chad  
1032 basin. *Journal of Geophysical Research: Atmospheres* 106, 3349-3356.
- 1033 Coward, M. P., Ries, A. C., 2003. Tectonic development of North African basins. Geological Society,  
1034 London, Special Publications 207, 61-83.
- 1035 Crouvi, O., Schepanski, K., Amit, R., Gillespie, A.R., Enzel, Y., 2012. Multiple dust sources in the  
1036 Sahara Desert: The importance of sand dunes. *Geophysical Research Letters* 39, L13401,  
1037 doi:10.1029/2012GL052145.
- 1038 Cvetković, V., Toljić, M., Ammar, N.A., Rundić, L., Trish, K. B., 2010. Petrogenesis of the eastern  
1039 part of the Al Haruj basalts (Libya). *Journal of African Earth Sciences* 58, 37-50.
- 1040 deMenocal, P., Ortiz, J., Guilderson, T., Adkins, J., Sarnthein, M., Baker, L., Yarusinsky, M., 2000.  
1041 Abrupt onset and termination of the African Humid Period: Rapid climate responses to gradual  
1042 insolation forcing. *Quaternary Science Reviews* 19, 347-361.
- 1043 Denkler, T., Franz, G., Schandelmeier, H., 1994. Tectonometamorphic evolution of the  
1044 Neoproterozoic Delgo suture zone, northern Sudan. *Geologische Rundschau* 83, 578-590.
- 1045 Dickinson, W.R., 1985. Interpreting provenance relations from detrital modes of sandstones. In:  
1046 Zuffa, G.G. (ed.), *Provenance of Arenites*. Reidel, Dordrecht, NATO ASI Series 148, 333-361.
- 1047 Dott, R.H., 2003. The importance of eolian abrasion in supermature quartz sandstones and the  
1048 paradox of weathering on vegetation-free landscapes. *The Journal of Geology* 111, 387-405.

- 1049 Dott, R.H., Byers, C.W., Fielder, G.W., Stenzel, S.R., Winfree, K.E., 1986. Aeolian to marine  
1050 transition in Cambro-Ordovician cratonic sheet sandstones of the northern Mississippi Valley,  
1051 U.S.A. *Sedimentology* 33, 345–367.
- 1052 Drake, N. A., Blench, R. M., Armitage, S. J., Bristow, C. S., White, K. H., 2011. Ancient watercourses  
1053 and biogeography of the Sahara explain the peopling of the desert. *Proceedings of the National*  
1054 *Academy of Sciences* 108, 458-462.
- 1055 Dutta, P.K., Zhou, Z., dos Santos, P.R., 1993. A theoretical study of mineralogical maturation of  
1056 eolian sand. In: Basu, A., Johnsson, M. (eds.), *Processes Controlling the Composition of Clastic*  
1057 *Sediments*. Geological Society of America, Special Paper 284, 203-209.
- 1058 East, A.E., Clift, P.D., Carter, A., Alizai, A., Van Laningham, S., 2015. Fluvial–eolian interactions  
1059 in sediment routing and sedimentary signal buffering: an example from the Indus Basin and Thar  
1060 Desert. *Journal of Sedimentary Research* 85(6), 715-728.
- 1061 Echikh, K., 1998. Geology and hydrocarbon occurrences in the Ghadames basin, Algeria, Tunisia,  
1062 Libya. Geological Society, London, Special Publications 132, 109-129.
- 1063 El-Baz, F., 1998. Sand accumulation and groundwater in the eastern Sahara. *Episodes* 21, 147-151.
- 1064 El-Baz, F., 2000. Satellite observations of the interplay between wind and water processes in the  
1065 Great Sahara. *Photogrammetric Engineering and Remote Sensing* 66(6), 777-782.
- 1066 Elbelrhiti, H., 2012. Initiation and early development of barchan dunes: A case study of the Moroccan  
1067 Atlantic Sahara Desert. *Geomorphology* 138, 181-188.
- 1068 Elshaafi, A., Gudmundsson, A., 2016. Volcano-tectonics of the Al haruj volcanic province, Central  
1069 Libya. *Journal of Volcanology and Geothermal Research* 325, 189-202.
- 1070 Ennih, N. Liégeois, J. P., 2001. The Moroccan Anti-Atlas: the West African craton passive margin  
1071 with limited Pan-African activity. Implications for the northern limit of the craton. *Precambrian*  
1072 *Research* 112, 291-304.
- 1073 Ennih, N., Liégeois, J.P., 2008. The boundaries of the West African craton, with special reference to  
1074 the basement of the Moroccan metacratonic Anti-Atlas belt. Geological Society, London, Special  
1075 Publications 297, 1-17.
- 1076 Fabre, J., Ba, H., Black, R., Caby, R., Leblanc, M., Lesquer, A., 1982. La chaîne Pan-Africaine, son  
1077 avant-pays et la zone de suture au Mali. Carte géologique et gravimétrique de l’Adrar des Iforas  
1078 au 1/500 000, notice and map. Direction nationale de la Géologie et des Mines, Bamako, 85.
- 1079 Feder, A., Zimmermann, R., Stollhofen, H., Caracciolo, L., Garzanti, E., Andreani, L., 2018. Fluvial-  
1080 aeolian sedimentary facies, Sossusvlei, Namib Desert. *Journal of Maps* 14(2), 630-643.
- 1081 Fekirine, B., Abdallah, H., 1998. Palaeozoic lithofacies correlatives and sequence stratigraphy of the  
1082 Saharan Platform, Algeria. Geological Society, London, Special Publications 132, 97-108.
- 1083 Feller, W., 1948. On the Kolmogorov-Smirnov limit theorems for empirical distributions. *Annals of*  
1084 *Mathematical Statistics* 19, 177-189.

- 1085 Feybesse, J.L., Milési, J.P., 1994. The Archaean/Proterozoic contact zone in West Africa: A mountain  
1086 belt of décollement thrusting and folding on a continental margin related to 2.1 Ga convergence  
1087 of Archaean cratons? *Precambrian Research* 69, 199-227.
- 1088 Fezaa, N., Liégeois, J.P., Abdallah, N., Cherfouh, E.H., De Waele, B., Bruguier, O., Ouabadi, A.,  
1089 2010. Late Ediacaran geological evolution (575–555 Ma) of the Djanet Terrane, Eastern Hoggar,  
1090 Algeria, evidence for a Murzukian intracontinental episode. *Precambrian Research* 180, 299-327.
- 1091 Fezaa, N., Liégeois, J.P., Abdallah, N., Bruguier, O., De Waele, B., Ouabadi, A., 2019. The 600 Ma-  
1092 old Pan-African magmatism in the In Ouzzal terrane (Tuareg Shield, Algeria): Witness of the  
1093 metacratonisation of a rigid block. *The Geology of the Arab World - An Overview*. Springer,  
1094 Cham., 109-148.
- 1095 Gabriel, K.R., 1971. The biplot graphic display of matrices with application to principal component  
1096 analysis. *Biometrika* 58, 453-467.
- 1097 Galehouse, J.S., 1971. Point counting. *Procedures in sedimentary petrology*. Wiley, New York, 385-  
1098 407.
- 1099 Gao, H., Bohn, T. J., Podest, E., McDonald, K.C., Lettenmaier, D.P., 2011. On the causes of the  
1100 shrinking of Lake Chad. *Environmental Research Letters* 6, 034021.
- 1101 Garzanti, E., 1991. Non-carbonate intrabasinal grains in arenites: Their recognition, significance and  
1102 relationship to eustatic cycles and tectonic setting. *Journal of Sedimentary Petrology* 61, 959-  
1103 975.
- 1104 Garzanti, E., 2017. The maturity myth in sedimentology and provenance analysis. *Journal of*  
1105 *Sedimentary Research* 87, 353-365.
- 1106 Garzanti, E., 2019. Petrographic classification of sand and sandstone. *Earth-Science Reviews* 192,  
1107 545-563.
- 1108 Garzanti, E., Andò, S., 2007. Plate tectonics and heavy-mineral suites of modern sands. In: Mange,  
1109 M.A., Wright, D.T. (eds.), *Heavy minerals in use*. Elsevier, Amsterdam, *Developments in*  
1110 *Sedimentology* 58, 741-763.
- 1111 Garzanti, E., Andò, S., 2019. Heavy Minerals for Junior Woodchucks. *Minerals* 9, 148,  
1112 doi:10.3390/min9030148.
- 1113 Garzanti, E., Vezzoli, G., 2003. A classification of metamorphic grains in sands based on their  
1114 composition and grade. *Journal of Sedimentary Research*, 73, 830-837.
- 1115 Garzanti E., Vezzoli G., Andò S., Castiglioni G., 2001. Petrology of rifted-margin sand (Red Sea and  
1116 Gulf of Aden, Yemen). *The Journal of Geology* 109, 277-297.
- 1117 Garzanti, E., Andò, S., Vezzoli, G., Dell’Era, D., 2003. From rifted margins to foreland basins :  
1118 investigating provenance and sediment dispersal across desert Arabia (Oman, UAE). *Journal of*  
1119 *Sedimentary Research* 73, 572-588.
- 1120 Garzanti E., Doglioni C., Vezzoli G., Andò S., 2007. Orogenic belts and orogenic sediment  
1121 provenances. *The Journal of Geology* 115, 315-334.

- 1122 Garzanti, E., Andò, S., Vezzoli, G., Lustrino, M., Boni, M., Vermeesch, P., 2012. Petrology of the  
1123 Namib Sand Sea: Long-distance transport and compositional variability in the wind-displaced  
1124 Orange Delta. *Earth-Science Reviews* 112, 173-189.
- 1125 Garzanti, E., Vermeesch, P., Andò, S., Vezzoli, G., Valagussa, M., Allen, K., Khadi, K.A., Al-  
1126 Juboury, I.A., 2013. Provenance and recycling of Arabian desert sand. *Earth-Science Reviews*  
1127 120, 1–19.
- 1128 Garzanti, E., Vermeesch, P., Andò, S., Lustrino, M., Padoan, M., Vezzoli, G., 2014a. Ultra-long  
1129 distance littoral transport of Orange sand and provenance of the Skeleton Coast Erg (Namibia).  
1130 *Marine Geology* 357, 25-36.
- 1131 Garzanti, E., Vermeesch, P., Padoan, M., Resentini, A., Vezzoli, G., Andò, S., 2014b. Provenance of  
1132 passive-margin sand (southern Africa). *The Journal of Geology* 122, 17-42.
- 1133 Garzanti, E., Andò, S., Padoan, M., Vezzoli, G., El Kammar, A., 2015a. The modern Nile sediment  
1134 system: Processes and products. *Quaternary Science Reviews* 130, 9-56.
- 1135 Garzanti, E., Resentini, A., Andò, S., Vezzoli, G., Vermeesch, P., 2015b. Physical controls on sand  
1136 composition and relative durability of detrital minerals during long-distance littoral and eolian  
1137 transport (coastal Namibia). *Sedimentology*, 62, 971-996, DOI: 10.1111/sed.12169.
- 1138 Garzanti, E., Al-Juboury, A.I., Zoleikhaei, Y., Vermeesch, P., Jotheri, J., Akkoca, D.B., Allen, M.,  
1139 Andò, S., Limonta, M., Padoan, M., Resentini, A., Rittner, M., Vezzoli, G., 2016. The Euphrates-  
1140 Tigris-Karun river system: Provenance, recycling and dispersal of quartz-poor foreland-basin  
1141 sediments in arid climate. *Earth-Science Reviews* 162, 107-128.
- 1142 Garzanti E., Vermeesch, P., Al-Ramadan, K.A., Andò, S., Limonta, M., Rittner, M., Vezzoli, G.,  
1143 2017. Tracing transcontinental sand transport: From Anatolia-Zagros to the Rub' al Khali Sand  
1144 Sea. *Journal of Sedimentary Research* 87, 1196-1213.
- 1145 Garzanti, E., Dinis, P., Vermeesch, P., Andò, S., Hahn, A., Huvi, J., Limonta, M., Padoan, M.,  
1146 Resentini, A., Rittner, M., Vezzoli, G., 2018a. Dynamic uplift, recycling, and climate control on  
1147 the petrology of passive-margin sand (Angola). *Sedimentary Geology* 375, 86-104.
- 1148 Garzanti, E., Vermeesch, P., Rittner, M., Simmons, M., 2018b. The zircon story of the Nile: Time-  
1149 structure maps of source rocks and discontinuous propagation of detrital signals. *Basin*  
1150 *Research* 30, 1098-1117.
- 1151 Garzanti, E., Dinis, P., Vermeesch, P., Andò, S., Hahn, A., Huvi, J., Limonta, M., Padoan, M.,  
1152 Resentini, A., Rittner, M., Vezzoli, G., 2018c. Sedimentary processes controlling ultralong cells  
1153 of littoral transport: Placer formation and termination of the Orange sand highway in southern  
1154 Angola, *Sedimentology* 65, 431-460.
- 1155 Garzanti, E., Vermeesch, P., Vezzoli, G., Andò, S., Botti, E., Limonta, M., Dinis, P., Hahn, A.,  
1156 Baudet, D., De Grave, J., Yaya, N.K., 2019a. Congo River sand and the equatorial quartz factory.  
1157 *Earth-Science Reviews* 197, 102918.
- 1158 Garzanti, E., Ghassemi, M.R., Limonta, M., Resentini, A., 2019b. Provenance of Karakum Desert  
1159 sand (Turkmenistan): Lithic-rich orogenic signature of central Asian dune fields. *Rivista Italiana*  
1160 *di Paleontologia e Stratigrafia* 125(1), 77-89.

- 1161 Garzanti, E., Liang, W., Andò, S., Clift, P.D, Resentini, A., Vermeesch, P., Vezzoli, G., 2020.  
 1162 Provenance of Thal Desert sand: Focused erosion in the western Himalayan syntaxis and  
 1163 foreland-basin deposition driven by latest Quaternary climate change. *Earth-Science Reviews*,  
 1164 207, 103220.  
 5
- 1165 Gasse, F., 2000. Hydrological changes in the African tropics since the Last Glacial Maximum.  
 1166 *Quaternary Science Reviews* 19, 189-211.  
 7
- 1167 Geyh, M.A., Thiedig, F., 2008. The Middle Pleistocene Al Mahrúqah Formation in the Murzuq Basin,  
 1168 northern Sahara, Libya: evidence for orbitally-forced humid episodes during the last 500,000  
 1169 years. *Palaeogeography, Palaeoclimatology, Palaeoecology* 257, 1-21.  
 9
- 1170 Ghienne, J.F., Desrochers, A., Vandenbroucke, T.R., Achab, A., Asselin, E., Dabard, M.P., Farley,  
 1171 C., Loi, A., Paris, F., Wickson, S., Veizer, J., 2014. A Cenozoic-style scenario for the end-  
 1172 Ordovician glaciation. *Nature Communications* 5, 1-9.  
 14
- 1173 Ghoneim, E., Robinson, C., El-Baz, F., 2007. Radar topography data reveal drainage relics in the  
 1174 eastern Sahara. *International Journal of Remote Sensing* 28, 1759-1772.  
 19
- 1175 Ghuma, M.A., Rogers, J.J.W., 1978. Geology, geochemistry, and tectonic setting of the Ben Ghnema  
 1176 batholith, Tebisti Massif, southern Libya. *Geological Society America Bulletin* 89, 1315–1358.  
 20
- 1177 Gischler, C.E., 1976. Hydrology of the Sahara. *Ecological Bulletins*, 83-101.  
 22
- 1178 Gossel, W., Ebraheem, A.M., Wycisk, P., 2004. A very large scale GIS-based groundwater flow  
 1179 model for the Nubian sandstone aquifer in Eastern Sahara (Egypt, northern Sudan and eastern  
 1180 Libya). *Hydrogeology Journal* 12, 698-713.  
 25
- 1181 Goudie, A.S., 2005. The drainage of Africa since the Cretaceous. *Geomorphology* 67, 437-456.  
 26
- 1182 Gower, J.C., 1975. Generalized procrustes analysis. *Psychometrika* 40, 33-51.  
 28
- 1183 Greenacre, M., 2017. Correspondence analysis in practice. CRC press, Boca Raton (FL), 327 p.  
 29
- 1184 Griffin, W.L., Powell, W.J., Pearson, N.J., O'Reilly, S.Y., 2008. GLITTER: data reduction software  
 1185 for laser ablation ICP-MS. *Laser Ablation-ICP-MS in the earth sciences*. Mineralogical  
 1186 association of Canada, short course series 40, 204-207.  
 31
- 1187 Grove, A.T., Warren, A., 1968. Quaternary landforms and climate on the south side of the Sahara.  
 1188 *The Geographical Journal* 134, 194-208.  
 32
- 1189 Haddoum, H., Guiraud, R., Moussine-Pouchkine, A., 2001. Hercynian compressional deformations  
 1190 of the Ahnet-Mouydir Basin, Algerian Saharan Platform: Far-field stress effects of the Late  
 1191 Paleozoic orogeny. *Terra Nova* 13, 220-226.  
 33
- 1192 Haug, G.H., Hughen, K.A., Sigman, D.M., Peterson, L.C., Röhl, U., 2001. Southward migration of  
 1193 the intertropical convergence zone through the Holocene. *Science* 293, 1304-1308.  
 34
- 1194 Hubert, J.F., 1962. A zircon–tourmaline–rutile maturity index and the interdependence of the  
 1195 composition of heavy mineral assemblages with the gross composition and texture of sandstones.  
 1196 *Journal of Sedimentary Petrology* 32, 440-450.  
 35



- 1197 Ingersoll, R.V., Bullard, T.F., Ford, R.L., Grimm, J.P., Pickle, J.D., Sares, S.W., 1984. The effect of  
1198 grain size on detrital modes: A test of the Gazzi-Dickinson point-counting method. *Journal of*  
1199 *Sedimentary Petrology* 54, 103-116.
- 1200 Jackson, S.E., Pearson, N.J., Griffin, W.L., Belousova, E.A., 2004. The application of laser ablation-  
1201 inductively coupled plasma-mass spectrometry to in situ U–Pb zircon geochronology. *Chemical*  
1202 *Geology* 211, 47-69.
- 1203 Jewell, A.M., Drake, N., Crocker, A.J., Bakker, N.L., Kunkelova, T., Bristow, C.S., Cooper, M.J.,  
1204 Milton, J.A., Breeze, P.S., Wilson, P.A., 2020. Three North African dust source areas and their  
1205 geochemical fingerprint. *Earth and Planetary Science Letters* 554, 116645,  
1206 doi.org/10.1016/j.epsl.2020.116645.
- 1207 Johnsson, M.J., 1993. The system controlling the composition of clastic sediments. In: Johnsson,  
1208 M.J., Basu, A. (eds.), *Processes controlling the composition of clastic sediments*. Geological  
1209 Society of America, Special Paper 284, pp. 1–19.
- 1210 Koren, I., Kaufman, Y.J., Washington, R., Todd, M.C., Rudich, Y., Martins, J.V., Rosenfeld, D.,  
1211 2006. The Bodélé depression: A single spot in the Sahara that provides most of the mineral dust  
1212 to the Amazon forest. *Environmental Research Letters* 1, 01400.
- 1213 Kruskal, J.B., Wish, M., 1978. *Multidimensional scaling*. Sage Publications, Newbury Park (CA),  
1214 Quantitative applications in the social sciences, Sage University Paper Series 07-011, 92 p.
- 1215 Krynine, P.D., 1941. Paleogeographic and tectonic significance of sedimentary quartzites. *Geological*  
1216 *Society of America Bulletin* 52, 1915–1916.
- 1217 Kuper, R., Kröpelin, S., 2006. Climate-controlled Holocene occupation in the Sahara: Motor of  
1218 Africa's evolution. *Science* 313, 803-807.
- 1219 Kuster, D., Liégeois, J.-P., 2001. Sr, Nd isotopes and geochemistry of the Bayuda Desert high-grade  
1220 metamorphic basement (Sudan): An early Pan-African oceanic convergent margin, not the edge  
1221 of the East Saharan ghost craton. *Precambrian Research* 109, 1–23.
- 1222 Lancaster, N., 1995. *Geomorphology of desert dunes*. Psychology Press.
- 1223 Lancaster, N., 2020. On the formation of desert loess. *Quaternary Research* 96, 105-122. 247.
- 1224 Liang, W., Garzanti, E., Andò, S., Gentile, P., Resentini, A., 2019. Multiminerall fingerprinting of  
1225 Transhimalayan and Himalayan sources to Indus-derived Thal Desert sand (central Pakistan).  
1226 *Minerals*, 9, 457; doi:10.3390/min9080457.
- 1227 Liégeois, J.P., 2019. A new synthetic geological map of the Tuareg Shield: An overview of its global  
1228 structure and geological evolution. In *The Geology of the Arab World - An Overview*. Springer,  
1229 Cham, 83-107.
- 1230 Liégeois, J.P., Black, R., 1987. Alkaline magmatism subsequent to collision in the Pan-African belt  
1231 of the Adrar des Iforas (Mali). *Alkaline Igneous Rocks* 30, 381-401.
- 1232 Liégeois, J.P., Black, R., Navez, J., Latouche, L., 1994. Early and late Pan-African orogenies in the  
1233 Air assembly of terranes (Tuareg Shield, Niger). *Precambrian Research* 67, 59-88.

- 1234 Liégeois, J.P., Latouche, L., Navez, J., Black, R., 2000. Pan-African collision, collapse and escape  
1235 tectonics in the Tuareg shield: Relations with the East Saharan Ghost craton and the West African  
1236 craton. *Journal of African Earth Sciences* 30, 53-53.
- 1237 Linnemann, U., Ouzegane, K., Drareni, A., Hofmann, M., Becker, S., Gärtner, A., Sagawe, A., 2011.  
1238 Sands of West Gondwana: An archive of secular magmatism and plate interactions—a case study  
1239 from the Cambro-Ordovician section of the Tassili Ouan Ahaggar (Algerian Sahara) using U–  
1240 Pb–LA-ICP-MS detrital zircon ages. *Lithos* 123, 188-203.
- 1241 Ludwig, K.R., 1998. On the treatment of concordant uranium-lead ages. *Geochimica et*  
1242 *Cosmochimica Acta* 62, 665-676.
- 1243 Mainguet, M., 1978. The influence of trade winds, local air-masses and topographic obstacles on the  
1244 aeolian movement of sand particles and the origin and distribution of dunes and ergs in the Sahara  
1245 and Australia. *Geoforum* 9, 17-28.
- 1246 Mainguet, M., Callot, Y., 1978. L'erg de Fachi-Bilma, Tchad-Niger: contribution à la connaissance  
1247 de la dynamique des ergs et des dunes des zones arides chaudes. Éditions du Centre national de  
1248 la recherche scientifique.
- 1249 Mainguet, M., Chemin, M.C., 1983. Sand seas of the Sahara and Sahel: An explanation of their  
1250 thickness and sand dune type by the sand budget principle. Elsevier, Amsterdam, *Developments*  
1251 *in sedimentology* 38, 353-363.
- 1252 Mattauer, M., Tapponier, P., Proust, F., 1977. Sur les mécanismes de formation des chaînes  
1253 intracontinentales: L'exemple des chaînes atlasiques du Maroc, *Bulletin de la Société Géologique*  
1254 *de France* 77, 521-526.
- 1255 Meftah, N., Mahboub, M.S., 2020. Spectroscopic characterizations of sand dunes minerals of El-  
1256 Oued (Northeast Algerian Sahara) by FTIR, XRF and XRD analyses. *Silicon* 12, 147-153.
- 1257 Meinhold, G., Morton, A.C., Fanning, C.M., Frei, D., Howard, J.P., Phillips, R.J., Strogon, D.,  
1258 Whitham, A.G., 2011. Evidence from detrital zircons for recycling of Mesoproterozoic and  
1259 Neoproterozoic crust recorded in Paleozoic and Mesozoic sandstones of southern Libya. *Earth*  
1260 *and Planetary Science Letters* 312, 164-175.
- 1261 Meinhold, G., Morton, A.C., Avigad, D., 2013. New insights into peri-Gondwana paleogeography  
1262 and the Gondwana super-fan system from detrital zircon U–Pb ages. *Gondwana Research* 23,  
1263 661-665.
- 1264 Middleton, N.J., Goudie, A.S., 2001. Saharan dust storms: nature and consequences. *Earth-Science*  
1265 *Reviews* 56, 179–204.
- 1266 Moreau, C., Demaiffe, D., Bellion, Y., Boullier, A.M., 1994. A tectonic model for the location of  
1267 Palaeozoic ring complexes in Air (Niger, West Africa). *Tectonophysics* 234, 129-146.
- 1268 Morton, A.C., Meinhold, G., Howard, J.P., Phillips, R.J., Strogon, D., Abutarruma, Y., Elgady, M.,  
1269 Thusu, B., Whitham, A.G., 2011. A heavy mineral study of sandstones from the eastern Murzuq  
1270 Basin, Libya: Constraints on provenance and stratigraphic correlation. *Journal of African Earth*  
1271 *Sciences* 61, 308-330.

- 1272 Muhs, D.R., 2004. Mineralogical maturity in dunefields of North America, Africa and Australia.  
1273 *Geomorphology* 59, 247-269.  
2
- 1274 Muhs, D.R., Bush, C.A., Stewart, K.C., Rowland, T.R., Crittenden, R.C., 1990. Geochemical  
1275 evidence of Saharan dust parent material for soils developed on Quaternary limestones of  
1276 Caribbean and western Atlantic islands. *Quaternary Research* 33, 157-177.  
7
- 1277 Muhs, D.R., Meco, J., Budahn, J.R., Skipp, G.L., Betancort, J.F., Lomoschitz, A., 2019. The antiquity  
1278 of the Sahara Desert: New evidence from the mineralogy and geochemistry of Pliocene paleosols  
1279 on the Canary Islands, Spain. *Palaeogeography, Palaeoclimatology, Palaeoecology* 533, 109245.  
12
- 1280 Muhs, D.R., Roskin, J., Tsoar, H., Skipp, G., Budahn, J.R., Sneh, A., Porat, N., Stanley, J.D., Katra,  
1281 I., Blumberg, D.G., 2013. Origin of the Sinai–Negev erg, Egypt and Israel: Mineralogical and  
1282 geochemical evidence for the importance of the Nile and sea level history. *Quaternary Science  
1283 Reviews* 69, 28-48.  
18
- 1284 Nance, R.D., Murphy, J.B., Strachan, R.A., Keppie, J.D., Gutiérrez-Alonso, G., Fernández-Suárez,  
1285 J., Quesada, C., Linnemann, U., D'lemos, R., Pisarevsky, S.A., 2008. Neoproterozoic-early  
1286 Palaeozoic tectonostratigraphy and palaeogeography of the peri-Gondwanan terranes:  
1287 Amazonian v. West African connections. *Geological Society, London, Special Publications* 297,  
1288 345-383.  
26
- 1289 Nicholson, S.E., Flohn, H., 1980. African environmental and climatic changes and the general  
1290 atmospheric circulation in late Pleistocene and Holocene. *Climatic change* 2, 313-348.  
29
- 1291 Nie, J., Stevens, T., Rittner, M., Stockli, D., Garzanti, E., Limonta, M., Bird, A., Andò, S., Vermeesch,  
1292 P., Saylor, J., Lu, H., Breecker, D., Hu, X., Liu, S., Resentini, A., Vezzoli, G., Peng, W., Carter,  
1293 A., Ji, S., Pan, B., 2015. Loess Plateau storage of Northeastern Tibetan Plateau-derived Yellow  
1294 River sediment. *Nature Communications*, 6, DOI: 10.1038/ncomms9511.  
36
- 1295 Pachur, H.J., Kröpelin, S., 1987. Wadi Howar: Paleoclimatic evidence from an extinct river system  
1296 in the southeastern Sahara. *Science* 237, 298-300.  
39
- 1297 Pang, H., Pan, B., Garzanti, E., Gao, H., Zhao, X., Chen, D., 2018. Mineralogy and geochemistry of  
1298 modern Yellow River sediments: Implications for weathering and provenance. *Chemical  
1299 Geology*, 488, 76-86.  
44
- 1300 Pinna, P., Calvez, J.Y., Abessolo, A., Angel, J.M., Mekoulou- Mekoulou, T., Mananga, G., Vernhet,  
1301 Y., 1994. Neoproterozoic events in Tchollire area: Pan-African crustal growth and geodynamics  
1302 in central-northern Cameroon (Adamawa and North Provinces). *Journal African Earth Sciences*  
1303 18, 347-353.  
50
- 1304 Prospero, J.M., 1996. Saharan dust transport over the North Atlantic Ocean and Mediterranean: An  
1305 overview. In: Guerzoni, S., Chester, R. (eds.), *The impact of desert dust across the  
1306 Mediterranean*. Springer, Dordrecht, 133-151.  
55
- 1307 Pye, K., Tsoar, H., 2008. *Aeolian sand and sand dunes*. Springer Science & Business Media.
- 1308 Resentini, A., Andò, S., Garzanti, E., 2018. Quantifying roundness of detrital minerals by image  
1309 analysis: sediment transport, shape effects, and provenance implications. *Journal of Sedimentary  
1310 Research* 88, 276–289.  
62

- 1311 Rittner, M., Vermeesch, P., Carter, A., Bird, A., Stevens, T., Garzanti, E., Andò, S., Vezzoli, G., Dutt,  
1312 R., Xu, Z., Lu, H., 2016. The provenance of Taklamakan desert sand. *Earth and Planetary Science*  
1313 *Letters* 437, 127-137.
- 1314 Rogers, J.W., Ghuma, M.A., Nagy, R.M., Greenburg, J.K., Fullagar, P.D., 1978. Plutonism in Pan-  
1315 African belts and the geologic evolution of northeastern Africa. *Earth Planetary Science Letters*  
1316 39, 109–117.
- 1317 Salze, D., Belcourt, O., Harouna, M., 2018. The first stage in the formation of the uranium deposit of  
1318 Arlit, Niger: Role of a new non-continental organic matter. *Ore Geology Reviews* 102, 604-617.
- 1319 Sarnthein, M., 1978. Sand deserts during glacial maximum and climatic optimum. *Nature* 272, 43-  
1320 46.
- 1321 Schandelmeier, H., Darbyshire, D.P.F., Harms, U., Richter, A., 1988. The E Saharan craton: Evidence  
1322 for pre-Pan-African crust in NE Africa W of the Nile. In: El-Gaby, S., Greiling, R.O. (eds.), *The*  
1323 *Pan-African belts of NE Africa and Adjacent areas*. Friedrich Vieweg and Sohn, 69-94.
- 1324 Selley, R.C., 1997. The sedimentary basins of northwest Africa: Stratigraphy and sedimentation. In:  
1325 Selley, R.C. (ed.), *Sedimentary Basins of the World 3, African Basins*. Elsevier, Amsterdam, 3-  
1326 16.
- 1327 Shaw, A., Goudie, A.S., 2002. Geomorphological evidence for the extension of the Mega-Kalahari  
1328 into south-central Angola. *South African Geographical Journal* 84, 182–194.
- 1329 Sláma, J., Košler, J., Condon, D.J., Crowley, J.L., Gerdes, A., Hanchar, J.M., Horstwood, M.S.,  
1330 Morris, G.A., Nasdala, L., Norberg, N., Schaltegger, U., 2008. Plešovice zircon—a new natural  
1331 reference material for U–Pb and Hf isotopic microanalysis. *Chemical Geology* 249, 1-35.
- 1332 Smith, B.J., Wright, J.S., Whalley, W.B., 2002. Sources of non-glacial, loess-size quartz silt and the  
1333 origins of “desert loess”. *Earth-Science Reviews* 59, 1-26.
- 1334 Stanistreet, I.G., Stollhofen, H., 2002. Hoanib River flood deposits of Namib Desert interdunes as  
1335 analogues for thin permeability barrier mudstone layers in aeolianite reservoirs. *Sedimentology*  
1336 49, 719–736.
- 1337 Stern, R.J., 1985. The Najd fault system, Saudi Arabia and Egypt: A late Precambrian rift- related  
1338 transform system? *Tectonics* 4, 497-511.
- 1339 Stern, R.J., Kröner, A., Reischmann, T., Bender, R., Dawoud, A.S., 1994. Precambrian basement  
1340 around Wadi Halfa: A new perspective on the evolution of the Central Saharan Ghost craton.  
1341 *Geologische Rundschau* 83, 564-577.
- 1342 Stevens, T., Carter, A., Watson, T.P., Vermeesch, P., Andò, S., Bird, A.F., Lu, H., Garzanti, E.,  
1343 Cottam, M.A., Sevastjanova, I., 2013. Genetic linkage between the Yellow River, the Mu Us  
1344 desert and the Chinese Loess Plateau. *Quaternary Science Reviews* 78, 355-368.
- 1345 Sutcliffe, J.V., Parks, Y.P., 1999. *The Hydrology of the Nile*. International Association of  
1346 Hydrological Sciences, Special Publication 5, 179 p.
- 1347 Suttner, L.J., Basu, A., Mack, G.H., 1981. Climate and the origin of quartz arenites. *Journal of*  
1348 *Sedimentary Petrology* 51, 1235–1246.

- 1349 Svendsen, J., Stollhofen, H., Krapf, C.B.E., Stanistreet, I.G., 2003. Mass and hyperconcentrated  
1350 flowdeposits record dune damming and catastrophic breakthrough of ephemeral rivers, Skeleton  
1351 Coast Erg, Namibia. *Sedimentary Geology* 160, 7–31.
- 1352 Swap, R., Garstang, M., Greco, S., Talbot, R., Källberg, P., 1992. Saharan dust in the Amazon Basin.  
1353 *Tellus B*, 44(2), 133-149.
- 1354 Swezey, C., 2001. Eolian sediment responses to late Quaternary climate changes: Temporal and  
1355 spatial patterns in the Sahara. *Palaeogeography, Palaeoclimatology, Palaeoecology* 167, 119-  
1356 155.
- 1357 Swezey, C.S., 2009. Cenozoic stratigraphy of the Sahara, northern Africa. *Journal of African Earth  
1358 Sciences*, 53, 89-121.
- 1359 Tegen, I., Schepanski, K., Heinold, B., 2013. Comparing two years of Saharan dust source activation  
1360 obtained by regional modelling and satellite observations. *Atmospheric Chemistry and Physics*  
1361 13(5), 2381–2390.
- 1362 Telbisz, T., Keszler, O., 2018. DEM-based morphometry of large-scale sand dune patterns in the  
1363 Grand Erg Oriental (Northern Sahara Desert, Africa). *Arabian Journal of Geosciences* 11, 382.
- 1364 Thomas, D.S.G., Shaw, P.A., 2002. Late Quaternary environmental change in central southern Africa:  
1365 new data, synthesis, issues and prospects. *Quaternary Science Reviews* 21, 783–797.
- 1366 Thomas, D.S.G., O'Connor, P.W., Bateman, M.D., Shaw, P.A., Stokes, S., Nash, D.J., 2000. Dune  
1367 activity as a record of late Quaternary aridity in the northern Kalahari: new evidence from  
1368 northern Namibia interpreted in the context of regional arid and humid chronologies.  
1369 *Palaeogeography Palaeoclimatology Palaeoecology* 156, 243–259.
- 1370 Thomas, R.J., Chevallier, L.P., Gresse, P.G., Harmer, R.E., Eglinton, B.M., Armstrong, R.A., De  
1371 Beer, C.H., Martini, J.E.J., De Kock, G.S., Macey, P.H., Ingram, B.A., 2002. Precambrian  
1372 evolution of the Sirwa window, Anti-Atlas orogen, Morocco. *Precambrian Research* 118, 1-57.
- 1373 Thusu, B., Mansouri, A., 1995. Reassignment of the Upper Amal Formation to Triassic and its  
1374 implications for exploration in southeast Sirte, Libya. First Symposium on Hydrocarbon Geology  
1375 of North Africa, London, 28–30 November, Abstracts 48.
- 1376 Vainer, S., Dor, Y.B., Matmon, A., 2018. Coupling cosmogenic nuclides and luminescence dating  
1377 into a unified accumulation model of aeolian landforms age and dynamics: The case study of the  
1378 Kalahari Erg. *Quaternary Geochronology* 48, 133-144.
- 1379 Vermeesch, P., 2013. Multi-sample comparison of detrital age distributions. *Chemical Geology* 341,  
1380 140-146.
- 1381 Vermeesch, P., 2018a. IsoplotR: A free and open toolbox for geochronology. *Geoscience Frontiers*  
1382 9, 1479-1493.



- 1383 Vermeesch, P., 2018b. Dissimilarity measures in detrital geochronology. *Earth-Science Reviews*,  
1384 178, 310-321. Statistical models for point-counting data. *Earth and Planetary Science Letters* 501,  
1385 112-118.
- 1386 Vermeesch, P., 2021. On the treatment of discordant detrital zircon U–Pb data. *Geochronology*  
1387 *Discussions*, 1-19. doi.org/10.5194/gchron-2020-38.
- 1388 Vermeesch, P., Garzanti, E., 2015. Making geological sense of ‘Big Data’ in sedimentary provenance  
1389 analysis. *Chemical Geology* 409, 20-27.
- 1390 Vermeesch, P., Resentini, A., Garzanti, E., 2016. An R package for statistical provenance  
1391 analysis. *Sedimentary Geology* 336, 14-25.
- 1392 Vermeesch, P., Rittner, M., Petrou, E., Omma, J., Mattinson, C., Garzanti, E., 2017. High throughput  
1393 petrochronology and sedimentary provenance analysis by automated phase mapping and  
1394 LAICPMS. *Geochemistry, Geophysics, Geosystems* 18, doi.org/10.1002/2017GC007109.
- 1395 Villeneuve, M., 2008. Review of the orogenic belts on the western side of the West African craton:  
1396 The Bassarides, Rokelides and Mauritanides. Geological Society, London, Special Publications  
1397 297, 169-201.
- 1398 Wang, Q., Spencer, C.J., Hamdidouche, R., Zhao, G., Evans, N.J., McDonald, B.J., 2020. Detrital  
1399 zircon U–Pb–Hf data from Cambrian sandstones of the Ougarta Mountains Algeria: Implication  
1400 for palaeoenvironment. *Geological Journal* 55(12), 7760-7774.
- 1401 Warner, T.T., 2009. *Desert Meteorology*. Cambridge University Press, 620 p.
- 1402 Wilson, I.G., 1971. Desert sandflow basins and a model for the development of ergs. *Geographical*  
1403 *Journal* 137(2), 180-199.
- 1404 Zhang, D., Narteau, C., Rozier, O., Du Pont, S.C., 2012. Morphology and dynamics of star dunes  
1405 from numerical modelling. *Nature Geoscience*, 5(7), 463-467.
- 1406 Zuffa, G.G., 1985. Optical analyses of arenites: influence of methodology on compositional results  
1407 In: Zuffa, G.G. (ed.), *Provenance of Arenites*. Reidel, Dordrecht, NATO ASI Series 148, 165-  
1408 189.